

University of Alberta

QUEST FOR QUIESCENT NEUTRON STAR LOW MASS X-RAY BINARIES
IN THE SMALL MAGELLANIC CLOUD

by

Md. Mizanul Huq Chowdhury

A thesis submitted to the Faculty of Graduate Studies and Research
in partial fulfillment of the requirements for the degree of

Master of Science

Department of Physics

© Md. Mizanul Huq Chowdhury

Spring 2011
Edmonton, Alberta

Permission is hereby granted to the University of Alberta Libraries to reproduce single copies of this thesis and to lend or sell such copies for private, scholarly or scientific research purposes only. Where the thesis is converted to, or otherwise made available in digital form, the University of Alberta will advise potential users of the thesis of these terms.

The author reserves all other publication and other rights in association with the copyright in the thesis and, except as herein before provided, neither the thesis nor any substantial portion thereof may be printed or otherwise reproduced in any material form whatsoever without the author's prior written permission.

Examining Committee

Craig Heinke, Physics

Sharon Morsink, Physics

Natasha Ivanova, Physics

Kambiz Moez, Electrical and Computer Engineering

ABSTRACT

We present the first spectral search for neutron stars (NSs) in low-mass X-ray binaries (LMXBs) between outbursts in the Small Magellanic Cloud (SMC). We identify and discuss candidate LMXBs in quiescence in the SMC using deep Chandra X-ray observations of two portions of the SMC. We produce X-ray color-magnitude-diagrams of XRSs of these two fields and identify 10 candidates for quiescent NS LMXBs. Spectral fitting and searches for optical counterparts rule out five, leaving five candidate quiescent NS LMXBs.

We estimate that we are sensitive to $\sim 10\%$ of quiescent NS LMXBs in our fields. Our fields include $4.4 \times 10^7 M_\odot$ of stellar mass, giving an upper limit of 10^{-6} LMXBs per M_\odot in the SMC. We place a lower limit on the average duty cycle of NS LMXBs as ~ 0.003 .

ACKNOWLEDGMENTS

Very first and foremost I have to thank my supervisor, Craig Heinke, without whom this thesis would not have been possible to be accomplished. He has been showing me the path on this research work as a mentor with his enlightened wisdom and knowledge. I appreciate his open door and always ready to help me on my all kinds of questions and curiosities. Its an honor for me to work with him as a graduate student.

My especial thanks to my colleague Clifton Price who has helped me to write down several *PERL* scripts that makes my work way easier. I also have to thank Tyron Woods, my office mate, for helping me to understand how to make figures and tables in Latex format.

My special thanks to my supervisory committee, Sharon Morsink, Natasha Ivanova and my external committee member Kambiz Moez for reading my thesis and also for their valuable remarks.

I also like to thank Sarah Derr who always have helped me all way of my Masters on any kind of academic needs.

I also need to mention the contributions of my parents and my family who always encourage and support me all through my life. Finally I am offering my heartfelt gratitude to almighty God who has given me the ability to finish this thesis on time.

Contents

Table of Contents	v
List of Figures	viii
List of Tables	ix
List of Symbols	xi
List of Acronyms	xi
1 Introduction	1
1.1 Stellar Life Cycles, And The Formation Of Compact Stars:	1
1.2 Interacting Binaries:	7
2 X-ray Observatories:	13
2.1 Early Work :	13
2.2 Einstein Satellite:	14
2.3 Chandra:	16
3 X-ray Binaries :	23
3.1 High Mass X-ray Binaries(HMXBs):	23

3.2	Low Mass X-ray Binaries(LMXBs):	26
3.3	Accretion Disks:	27
3.4	Transient Behavior:	28
3.5	LMXBs In Quiescence:	29
3.6	Populations Of Bright XRBs In Our Galaxy:	30
3.7	The Total Number Of LMXBs, qLMXBs, And Duty Cycles:	31
3.8	Globular Cluster XRBs:	33
3.9	LMXBs In Other Galaxies:	36
3.10	Known XRBs In The Magellanic Clouds:	37
4	X-ray Analysis:	40
4.1	The Chandra Deep Fields Of The SMC:	40
4.2	Data Reprocessing And Background Removal:	42
4.3	Source Detection:	45
4.4	ACIS_EXTRACT Data Extraction:	45
5	Results:	53
5.1	X-ray Color Magnitude Diagrams:	53
5.2	Spectral Fitting Of Candidates:	57
5.3	Comparison With Optical Counterpart Lists:	66
5.4	The X-ray To Optical Flux Ratio:	67
6	Constraints On The Quiescent NS LMXB Population Of The SMC:	69
6.1	Fraction Of Quiescent NS LMXBs Detectable:	70
6.2	Computation Of Stellar Mass In SMC Deep Fields:	70
6.3	Duty Cycle Of The Quiescent NS LMXBs:	72

7 Conclusion:

74

Bibliography

76

List of Figures

2.1	Chandra Telescope	19
2.2	The Science Instruments of Chandra Telescope	21
3.1	X-ray Binary System	25
3.2	Small Magellanic Cloud	39
4.1	Image of DF1 Chandra Data	43
4.2	Image of DF2 Chandra data	44
4.3	Overview of the AE steps	46
5.1	XCMD of DF1	55
5.2	XCMD for DF2	56
5.3	Power-law fit	59
5.4	Power-law+nsatmos fit	60
5.5	MEKAL fit	61

List of Tables

1	List Of Symbols	x
4.1	Observations	41
4.2	Luminosities and Counts of the DF1 XRSs	48
4.3	Luminosities and Counts of the DF1 XRSs	49
4.4	Luminosities and Counts of the DF1 XRSs	50
4.5	Luminosities and Counts of the DF2 XRSs	51
4.6	Luminosities and Counts of the DF2 XRSs	52
5.1	Luminosities and Counts of the candidates	63
5.2	Spectral model parameters	64
5.3	Spectral model parameters -continued-	65

Table 1. List Of Symbols

Symbols	Meaning
M_{\odot}	Solar mass; $1M_{\odot} = 1.98 \times 10^{33}$ Kgs
L_{\odot}	Solar luminosity; $1 L_{\odot} = 3.83 \times 10^{33}$ erg/s
L_x	X-ray Luminosity
F_x	X-ray flux
F_{opt}	Optical flux
Myr	Million years
Gyr	Giga years
pc	parsec; $1\text{pc} = 3.08 \times 10^{19}$ cm
G	Unit of Magnetic Field in CGS
J	Color magnitude in Infra Red
M_V	Absolute Visual Magnitude
V	Visual Magnitude
τ	Life time

List Of Acronyms

XRB X-ray Binaries

XRS X-ray Sources

LMXB Low Mass X-ray Binaries

NS Neutron Star

SMC Small Magellanic Cloud

LMC Large Magellanic Cloud

CV Cataclysmic Variable

WD White Dwarfs

IPs Intermediate Ploars

HEAO High Energy Astrophysics Observatory

SNR Signal-to-Noise Ratio

CXO Chandra X-ray Observatory

DC Duty Cycle

GCs Globular Clusters

DF Deep Field

CIAO Chandra Interactive Analysis of Observations

DEC Declination

RA Right Ascension

Exp. Time Exposure Time

XSPEC An X-ray Spectral fitting Package

AE ACIS Extract

ACIS Advanced CCD Imaging Spectroscopy

CMD Color Magnitude Diagram

OGLE Optical Gravitational Lensing Experiment

MCPS Magellanic Clouds Photometric Survey

2MASS Two Micron All Sky Survey

HST Hubble Space Telescope

AGN Active Galactic Nuclei

Chapter 1

Introduction

1.1 Stellar Life Cycles, And The Formation Of Compact Stars:

Stars have always been an object of curiosity to humans, from primitive ages to the modern astronomical era. We now know how a star is born, spends its various stages of life, and eventually ends in a dramatic death, or slow, silent doom. The exotic dense stars known as white dwarfs, neutron stars and black holes are together referred to as compact objects, or compact stars, for their high densities. These are the evolutionary endpoints of stars on their long, eventful lives, which we have summarized here.

Stars are formed by the contraction of interstellar cloud of gases under their own gravity. The formation of stars has been going on continuously for more than 10 billion years, since the time when our galaxy took its shape. Gravity compresses the low density, large cold clouds of gas of the interstellar medium into small, high-density,

hot stars. The epic begins with overcoming three constraints—thermal motion among the atoms and molecules of the gas, the interstellar magnetic field, and the increase in rotation that resists contraction. However, a passing shock wave like supernova explosions, the ultraviolet radiation of very hot stars, the collision of molecular clouds, or compression of molecular clouds by passage through a spiral arm of the galaxy, triggers the beginning of the collapse. In the first stage, the gravity of a dense cloud of gas and dust overcomes the resisting forces of atoms' thermal motion and magnetic pressure. This creates a high-density contracting core, surrounded by a cocoon of lower density, dusty, optically thick infalling clouds which hides the baby star's formation from our view. The angular momentum of the cloud core forces much of the matter to settle into a protostellar disk, which accretes onto the protostar, and is also believed to be the womb of planets. Eventually the protostar's increasing central density and pressure ignite fusion of hydrogen in its core, and the (still relatively large, low-density) protostar begins to emit substantial infrared luminosity. However, at this stage the star is still contracting, and material is still accreting. The protostar continues to contract until the pressure produced by its fusion luminosity becomes sufficient to balance the pull of gravity, bringing the star to a stable configuration. The locus of stable core hydrogen-burning conditions for stars of various masses are known as the main sequence. The star continues to fuse hydrogen into helium for a long, stable, hydrogen-fusion life. But this is not the happy ending of the story.

Stars are not eternal, though they enjoy millions or billions of years of luminous life, as majestic beacons twinkling across thousands of parsecs in the cosmos. Eventually the star exhausts hydrogen in its core. More massive stars require much higher central temperatures to support themselves, and thus much higher luminosities, overwhelming their higher mass—thus the more massive the star, the shorter its lifetime

will be. When hydrogen nears exhaustion in a star's core, the core pressure drops, and the core begins to contract. This contraction increases the central temperature and pressure, and brings material just outside the core up to temperatures capable of hydrogen fusion. As the core shrinks, its pressure is provided increasingly by degenerate pressure—two electrons are unable to share the same quantum state—rather than by thermal gas pressure. As the star fuses hydrogen in the outer core, the star's total luminosity increases, resulting in expansion of the star's outer layers. This increase in the star's luminosity and radius (and decline in surface temperature) marks the star's departure from the main sequence, to become a “red giant”. As the star exhausts its fuel, gravity overcomes all its opponent forces and leads the star to its doom.

Massive stars reach higher core temperatures allowing them to fuse other elements, but it just delays their end; the final smile is for gravity. Very low mass stars ($< 0.4M_{\odot}$) on the main sequence use their fuel very slowly; these red dwarfs are predicted to have a lifetime of up to a trillion years. The red dwarfs are completely convective (their entire interior is continually mixed) which results in uniform production of helium through the stars by fusion of hydrogen. But they can never ignite helium fusion, and so slowly meet their uneventful death. Proxima Centauri, the nearest star (though fainter than can be seen by the eye), is such a red dwarf.

The stars with mass $0.4M_{\odot} - 4M_{\odot}$, including our sun, reach core temperatures capable of fusing helium during their red giant stages. The initial ignition of helium occurs when the core is degenerate (pressure provided by electron degeneracy), so the temperature increase does not immediately expand the core; this leads to a “helium flash” of substantial energy output, which re-inflates the core and initiates a period of helium burning. When the helium fuel is consumed in the core, the core contracts again, and helium begins fusing in a shell around the core, expanding the star's outer

layers again as an “asymptotic giant branch” star. Slightly more massive ($> 4M_{\odot}$) stars compress their cores to higher densities and thus higher temperatures, igniting carbon fusion to produce oxygen along with neon and magnesium.

Due to the energy released by the contracting core, and the energy generated in the hydrogen and helium-fusing shells, the star’s envelope expands, producing a large red giant with a radius as large as the earth’s orbit and a surface temperature as cool as 3000 K. This envelope is loosely bound to the star, and blows away in a stellar wind, which can be later observed as a “planetary nebulae”. The core of the star is thus revealed, called now a white dwarf, composed largely of the final stages of the burning process (helium, carbon/oxygen, or oxygen/magnesium/neon, depending on the initial mass of the star). Their degenerate condition permits densities of 10^6 g cm^{-3} , a million times the average density of the Sun. The extremely high surface gravity of white dwarfs, $\sim 100,000$ times that of earth, causes sedimentation; heavier atoms in the atmosphere sink and leave the lightest gases (H, He) on the surface. White dwarfs do not generate energy, but only radiate their heat energy into space, gradually cooling into invisibility after billions of years. Sirius B, only 2.6 pc away from us, is the nearest white dwarf.

Stars with masses $> 11M_{\odot}$ have a different lifeline. Their higher mass induces higher temperatures and pressures in their cores, starting additional stages of fusion, from oxygen to silicon, sulfur and beyond. When the fusion reaches the production of iron, further fusion requires energy input rather than output, so the stellar core stops producing energy, and begins to collapse. Pressure from degenerate electrons is unable to continue increasing with density when the electron velocities approach the speed of light. This leads to gravity overwhelming degenerate electron pressure in massive stellar cores, over $\sim 1.4 M_{\odot}$ (the Chandrasekhar limit). The collapse can be halted

by the degeneracy pressure of protons and neutrons against one another. During the collapse, electrons are forced to combine with protons, producing a compact object composed mostly of neutrons—a neutron star. The collapse of an Earth-sized stellar core to a ~ 20 -km diameter neutron star releases huge quantities of energy, $\sim 10^{53}$ ergs. Much of this energy is released in the form of neutrinos, but 1% of the energy is captured by the star's outer layers, expelling them at high velocities. Energy deposited by a shock into the star's outer layers, plus the decay of radioactive elements, produce a bright optical display from the expanding outer layers that we call a supernova. The outer layers of the star, moving at high velocities (≥ 10000 km/s), remain visible for thousands of years as an expanding and cooling supernova remnant.

Neutron stars (NSs) have masses of 1.2 to $> 2 M_{\odot}$, and are a few times denser than atomic nuclei ($\sim 10^{15}$ g cm $^{-3}$). They have radii of ~ 12 km, and therefore extremely strong surface gravitational fields. The angular momentum of the NS is conserved as it collapses, so they spin very rapidly (several times a second at birth). The magnetic flux is also conserved as they collapse, producing high magnetic fields, perhaps a trillion times stronger than the sun's. Pulsars, lighthouses in the dark cosmos, are spinning NSs emitting radiation from their magnetic poles which sweeps around the sky as they spin. We detect this as pulses when their beam sweeps over us, as sailors in the vast ocean are swept by the light from the lighthouse. The intense, rapidly rotating magnetic field of neutron stars generates a powerful electric field which accelerates charged particles ripped from the NS surface. These relativistic particles emit gamma-rays and extremely bright, coherent radio emission from above the magnetic poles of the NS. Pulsars gradually slow down, through the emission of magnetic dipole radiation and the acceleration of charged particles, until the electric

fields become too weak to power the pulsar emission mechanism, at ages of about a million years. Some NSs experience a second life, if they were born in a binary star system which is not disrupted by the supernova explosion. Such NSs may be able to pull matter from their companion star, experiencing accretion and producing strong X-ray sources (see the chapter 3 below).

One more tale of gravity's climax remains; black holes. About 200 years ago John Michell, a Cambridge cleric, suggested that massive objects could have escape velocities so high that even photons cannot escape from their immense gravitational attraction. Coincidentally, Einstein's theory of gravity identifies this same criterion (mass condensed within a critical "Schwarzschild" radius $R_S = 2\frac{GM}{c^2}$) as "black holes", regions of spacetime where no outward paths are possible for either matter or radiation. If a neutron star accumulates a mass more than $\sim 3M_\odot$, the pressure of degenerate neutrons cannot balance gravity (similar to the failure of degenerate electrons above). Thus a complete gravitational collapse of the star results, leaving (naively) a zero radius object, a singularity. No information can emerge from the region around this point where the escape velocity is greater than that of light, the event horizon of the black hole. This is a black hole-totally blacked out from us.

Black holes themselves are invisible, but matter falling into such mysterious holes will be accelerated by gravity to enormous speeds approaching that of light. Interactions among material approaching the hole can therefore lead to the release of large quantities of energy at high temperature, producing intense sources of X-rays before they cross the event horizon. Binary systems containing black holes feeding from their companion star could thus be detected across our galaxy, and indeed several such systems are known. Cygnus X-1 was the first such candidate black hole, and is now known to be a high-mass (20-40 M_\odot) star and black hole (of mass $\sim 9M_\odot$)

orbiting each other every 5.6 days.

Stars are born in the wombs of cocoons, and enjoy millions or billions of years of luminous life before excitement comes in their calm life. Some just experience the white dwarf ending, some lucky ones flourish as neutron stars for their exotic finish, and a very few disappear into a new realm of reality through the ultimate black hole doom. This is the story of stars—a story that tells the victory of gravity, the weakest among the four fundamental forces, over everything of this boundaryless cosmos. [1–3].

1.2 Interacting Binaries:

Binary star systems consist of two stars that are orbiting each other around their common center of mass. More than half of all stars are in binaries, and they produce some of the most exotic astrophysics. Analysis of these systems can provide us with accurate measurements of stellar parameters such as their masses and densities. Binary stars can be detected in many ways; as visual binaries (where the two stars can be resolved with telescopes), astrometric binaries (where one star is much brighter, and its wobbling motion across the sky, pulled by the other star, can be resolved), eclipsing binaries (the stars periodically block part of the light from the other from reaching Earth), and spectroscopic binaries (where the spectral lines can be seen to shift, due to the velocities of the stars in their orbits) [2]. Eclipsing, spectroscopic binaries allow measurements of the true sizes, masses, and thus densities of stars. These binary systems reveal the facts that giants and supergiants are not immensely massive as their gigantic size might suggest, while tiny white dwarfs are extremely dense stars. The stellar density parameter classifies the stars into three groups: the

sun-like density of most main sequence stars, very-low-density stars like giants and supergiants, and high-density stars like white dwarfs. This density-dependent classification arises originally from observations using binary stars, giving us the ability to understand their internal stellar structures. [2].

Many interacting binary systems can be identified as X-ray sources. Such systems can be divided into two groups; those where the X-ray emission is due to mass transfer, and those where the X-ray emission is an enhancement of stellar chromospheric activity by the increased rotation of a star in a close binary. The latter category, 'chromospherically active binaries' or hereafter just 'active binaries', are binaries where the two stars are close enough together (the rotation period is less than a few days) that they are tidally locked (each turns one face to the other). Normal cool main-sequence stars produce X-rays in their coronae through the reconnection of magnetic field loops. This turbulence in the star's magnetic field is thought to be generated by a dynamo mechanism in the star's convection zone. The stellar X-ray luminosity is thus determined by the star's rotation rate, which drives the dynamo [4]. Typically stars slow down as they age, losing angular momentum by the stellar wind that flows from their corona [5]. Thus most old (billions of years) stars are weak X-ray sources, with X-ray luminosity $L_X < 10^{29}$ erg/s. But stars in tidally locked binaries are forced to rotate at higher rates, and thus produce more X-ray emission, with some active binaries reaching $L_X = 10^{31}$ erg/s or more. Although these systems do not reach the X-ray luminosities of mass-transferring systems with neutron stars or black holes (where L_X reaches 10^{36} erg/s or more), these systems are much more common, and make up the majority of X-ray sources found in our galaxy seen in individual X-ray observations with the Chandra X-ray Observatory.

Mass-transferring binaries are in such close orbits (often less than a day) that

material from one star is captured by the other star, either from the donor star's wind or through 'Roche-lobe overflow'. Compact objects orbiting stars with strong stellar winds can pull enough gas from the wind by their gravitational attraction to produce observable signs of accretion (described below). The Roche lobes for a binary star system are the figure-eight shaped equal gravitational potential surfaces that encompass the two stars. The central point, the inner Lagrangian point, feels equal gravitational pull from both stars.

If either star's surface crosses the inner Lagrangian point, matter from that star starts to flow onto the other one. Stars fill their Roche lobe potential by expanding (e.g. evolving towards a red giant), or by shrinking of their orbit through loss of angular momentum (here the stars stays the same size, but its Roche lobe shrinks along with the orbit). When a star fills its Roche lobe, matter at the inner Lagrangian point feels equal attraction from the two stars, and some of it flows towards the compact star (the accretor star; the other star is the donor star). Due to the conservation of angular momentum, the matter does not fall directly onto the compact accretor, rather the matter initially goes into orbit around the accretor. The stream of gas intersects other streams of gas orbiting around the accretor, leading to exchange of angular momentum and loss of energy to heat and radiation. The material which loses angular momentum spirals closer to the accretor, that which gains moves farther out, creating a disk of gas called an accretion disk. The gas in the disk gradually becomes very hot because of frictional (and magnetohydrodynamic viscosity) between different gas elements of the disk. The inner portion of the disk can reach maximum temperatures above 1,000,000 K, producing X-ray photons.

Mass transfer in binary systems is a critical piece of binary evolution. Depending on the star which is accumulating mass through the mass transfer phenomena we can

get different results: if the accretor star is a main sequence star, the system is an Algol-type binary, if it is a white dwarf we find a cataclysmic variable (CV), leading to thermonuclear fusion reactions novae and type Ia supernovae, while a neutron star or black hole as the accretor gives a system called an X-ray binary (XRB). [6]. The extremely luminous X-ray emission produced in XRBs is produced by material falling down the deep potential well of these compact objects [7]. I describe Algols and CVs below, and X-ray binaries in the chapter 3.

Algol systems are named after Beta Persei, or Algol, ~ 28.5 parsecs from us, which is an eclipsing binary. Algol systems generated a paradox, which can be understood when considering mass transfer. The puzzle was that the lower mass donor star was observed to be on the giant branch, while the massive accretor is still on the main sequence. This was abnormal, since a more massive star should expand earlier and evolve more rapidly than a less massive one (in a binary system, the two stars must be the same age). This problem is solved when we consider mass transfer, as the more massive one evolves and expands first, which fills up its Roche lobe and causes it to lose mass through the inner Lagrangian point to the lower mass accretor, which gradually gains mass until it is more massive, while less evolved, than the donor [2].

CVs (Cataclysmic Variables) are binary systems where a white dwarf accretes mass from a lower mass (typically red dwarf) star, with a separation of less than a few solar radii [8]. Depending on the white dwarf's magnetic field the accretion happens in one of two ways: for white dwarfs with low magnetic fields, the accretion disks continues down to the equator of the WD. If the WD has a strong magnetic field, the incoming matter, which is ionized, is forced to follow the field lines and land on the magnetic poles of the white dwarf. In magnetic CVs the magnetic field of the white dwarf controls the accretion flow which has a sheared disk, for the case of

Intermediate polars (IPs), or not any disk, for polar or AM Her system. In the case of Polar CVs orbital period of the white dwarf is locked with the rotation due to their strong enough magnetic field while the WD rotates faster due to less strong magnetic field for the case of IPs. EE Eri, AR UMa, AM Her, QQ Vul, Ex Hya, V1223 Sgr are some examples of magnetic CVs [1].

The loss of angular momentum from outflowing stellar winds driven by magnetic activity (mentioned above) also affects binary stars, by reducing their orbital period (this is called magnetic braking). In CVs, the transfer of matter from the lower-mass donor to the higher-mass accretor tends to expand the orbit, enlarging the Roche lobe and thus tending to stop mass transfer. A mechanism to lose angular momentum from the binary, however, shrinks the orbit, and forces matter to continue flowing to the accretor—the rate of mass transfer is determined by the rapidity of the angular momentum loss.

CVs with periods above 3 hours lose angular momentum principally through magnetic braking, driven by the stellar wind which is in turn driven by the magnetic activity of the star. However, stars small enough ($\sim 0.4M_{\odot}$) to fill their Roche lobe at an orbital period of 3 hours are just at the point of being convective throughout the star, as the convection zone includes more of the star for smaller stars. Below 3 hours, the magnetic activity of the star (driven by convection) is thought to change, and it becomes fully convective and its mass loss stops. However, angular momentum loss continues through gravitational radiation, so the CV's orbit slowly shrinks until the donor star makes contact with its Roche lobe again. Since the star has shrunk, it does not fill its Roche lobe again until it reaches an orbital period of about 2 hours, leaving the period gap in which CVs are not seen to transfer matter [9].

After this, the CV continues to transfer matter, driven by gravitational radiation

rather than faster magnetic braking, therefore at lower mass transfer rates. As the donor continues to lose mass, it eventually reaches a mass of $\sim 0.08 M_{\odot}$, the minimum mass for a star to burn hydrogen, at an orbital period of about 78 minutes. Below this mass, a hydrogen-rich donor is supported not by fusion but by degenerate electron pressure, and is considered a “brown dwarf”. Degenerate stars expand in response to mass loss (contrary to normal stars which shrink). This allows the donor to maintain contact with its Roche lobe, and thus continuation of mass transfer, as orbital separation increases. Thus the orbital period reaches a minimum value near 78 minutes, and less massive donors have wider orbits. Extremely old CVs will have tiny brown dwarf companions at periods of a few hours, transferring mass at extremely slow rates, and will be extremely difficult to observe. This depiction of the evolution of CV systems is generally supported by observations of populations of CVs (though there are problems in some of the details), and is thought to be generally applicable to X-ray binary systems as well. [10, 11]

Chapter 2

X-ray Observatories:

2.1 Early Work :

X-ray observations opened a new, wonderful window on our cosmos. Astronomical X-rays cannot pass through the Earth's atmosphere without being absorbed. The brightest cosmic X-rays, in the photon energy range of 0.5-5.0 keV, can be easily stopped by a thin layer of air. Mountain tops, simple balloons and even airplanes do not go high enough to perform most X-ray observations, so we need to go beyond our atmosphere. In the late 1950s and 1960s, rockets were built to carry X-ray detectors above our atmosphere. V2 rockets were the pioneers which launched by the US NRL (Naval Research Lab) found that the sun was a strong source of UV and X-ray radiation. Cosmic X-rays from beyond our solar system were first detected by an American Science and Engineering (AS&E) rocket group led by Riccardo Giacconi on 18 June 1962. Though the main aim of the AS&E mission was to detect X-ray emissions reflecting back from the lunar surface, instead they detected cosmic X-rays from a powerful X-ray source later named Sco X-1, the earliest X-ray source in constellation

Scorpius. This unexpected discovery ignited enthusiasm among astronomers and the X-ray astronomy era begun. The Crab Nebula, a young supernova remnant, was identified in 1964 by George Clark of MIT with a ballon-borne detector.

Uhuru which means 'freedom' in Swahilli language was the first X-ray astronomy satellite, launched (by NASA) from the coast of Kenya in 1970. Its long duration in space (vs. rocket flights) allowed the first comprehensive and uniform all sky-survey. Uhuru had a sensitive enough detector to detect X-ray sources 10 times fainter than the dimmest previously known sources, identifying 339 X-ray sources. The first High Energy Astronomy Observatory, HEAO-I, launched (by NASA) in 1977, performed an all-sky survey on the energy band 0.2 keV - 10 keV and catalogued 842 X-ray sources. It could measure the spectra of sources with the diffusive background and its better angular resolution allowed identification of hundreds of optical counterparts for X-ray sources. In 1983 EXOSAT (European X-ray Observatory SATelite) was launched by ESA (European Space Agency), with a large elliptical orbit of 30 earth radii that made it possible to observe X-ray sources continuously for up to 76 hours, vs. 45 minutes in Uhuru's low-Earth orbit. Discovery of the quasi-periodic oscillations in LMXBs and X-ray pulsars, and measuring emission lines of iron in galactic and extra-galactic sources were some of its major achievements. [1] ¹ .

2.2 Einstein Satellite:

In 1978, the first high resolution X-ray telescope, HEAO-2 or the Einstein Telescope, was launched by scientists from the Harvard-Smithsonian Center for Astrophysics, Columbia University, NASA/Goddard Space Flight Center, and MIT. For the first

¹<https://heasarc.gsfc.nasa.gov/docs/hea01/hea01.html>

time this mission used optical focusing with imaging detectors with an angular resolution of a few arcseconds and a 10' field-of-view. Its sensitivity was 100 times better than the any previous X-ray Astronomy missions. Einstein's payload had a high resolution X-ray telescope and its focus was arranged to be placed over any of four instruments: the High Resolution Imaging (HRI) detector, a digital X-ray camera with a high spatial and temporal resolution over 25' central of the focal plane; the broader field Imaging Proportional Counter (IPC), a position sensitive proportional counter that had good efficiency and covered the entire focal plane with $\sim 40''$ of best spatial resolution; the Solid State Spectrometer (SSS), consisting of a cryogenically cooled Si(Li) detector at the X-ray telescope's focus with 128 energy channel resolution; and the Focal Plane Crystal Spectrometer (FPCS), a Bragg crystal spectrometer designed with 6 various kind of crystal diffractors and proportional counters. A Monitoring Proportional Counter (MPC) was coaligned with the telescope for observing the volatility of the brighter X-ray sources and had an energy resolution of ~ 20 at 6 keV. Einstein detected stellar coronal emission that was much stronger than expectations, and it also detected X-ray jets emitted from Cen A and M87 aligned with radio jets. With a Guest Observer Program Einstein was the pioneer in sharing its facility to a large astronomical community, devising projects to use it for that

its designers didn't think of ². Other significant missions included Granat (Russian, 1989-1998) spacecraft with two telescopes to observe hard X-ray sources and γ -ray bursts. ROSAT (The ROentgen SATellite, 1990-1999) was a German, UK & US collaboration that was 1000 times more sensitive than Uhuru, which provided the deepest soft X-ray and extreme UV all-sky survey. ASCA (Advanced Satelite for Cosmology and Astrophysics, Japanese, 1993-2001) for the first time used CCD detectors

²https://heasarc.gsfc.nasa.gov/docs/einstein/heao2_about.html

(now standard) for X-ray astronomy, allowing substantial advances in spectral resolution and discoveries such as iron lines redshifted by their close approach to spinning black holes. The Rossi X-ray Timing Explorer (RXTE) mission (1995-today) has fast timing capability, the ability to slew quickly to new opportunities, and the largest effective area of any X-ray telescope, permitting it to make major discoveries in the timing of X-ray binaries, including the detection of the neutron star spin period in over a dozen X-ray binaries. BeppoSAX (Italian, 1996-2002) performed broad band spectroscopy (0.1-300 keV) and provided the first accurate positions of gamma-ray bursts, leading to their identification as distant cosmic explosions.

2.3 Chandra:

In 1999 the Chandra X-ray Observatory (CXO), was launched to a high elliptical orbit by Space Shuttle Columbia. Its excellent combination of sensitive detectors and precisely machined mirrors opened a wide new window to observe and study the origin, structure and evolution of the cosmos in more detail than ever before. It was named in honor of the late (Indian origin) American Nobel Laureate Dr. Subrahmanyan Chandrasekhar. It has three major components: (a) the X-ray telescope, (b) the science instruments and (3) the spacecraft. ^{3,4}. a) The X-ray telescope: The HRMA (High Resolution Mirror Assembly) and an optical bench are the prime elements of the telescope system (Chandra Proposers' Observatory guide version 7.0). The HRMA consists of four concentric grazing-incidence X-ray telescopes focusing the X-rays on one of the specific detectors. The telescope system includes four pairs of high-resolution mirrors. As X-rays have very high-energy X-ray photons easily penetrate

³http://chandra.harvard.edu/about/axaf_mission.html

⁴ <http://www.shuttlepresskit.com/sts-93/payload45.htm>

normal mirrors. So special nearly-cylindrical and super polished mirrors were made to the smoothness of a few atoms and coated with the super reflective rare metal, iridium. These are the smoothest, largest and cleanest mirrors ever created. The biggest mirror among these eight has a diameter of 4 feet and length of 3 feet⁵. These mirrors were assembled on a supportive stand (the HRMA) and aligned with superb accuracy. The precision of the alignment from one end to the other of the assembly is about one-fiftieth the width of a human hair⁶. To maintain the constant temperature of the devices inside the telescope system, the whole telescope is coated with highly reflective multi-fold insulation. This temperature precision keeps the mirrors from any kind of distortion through expansion or contraction. The mirrors were tested at the Marshall Space Flight Center, showing that Chandra has the ability to create X-ray images 25 times sharper⁷ and thus detect sources 20-50 times fainter than any previous X-ray telescope⁸. The resolution of the telescope is so precise that it has the equivalent ability to read the text of a newspaper from half a mile away.

(b) The science instruments: Four scientific instruments are connected with the mirrors to analyze X-rays from cosmic sources. Two are on the focal plane: ACIS and HRC; the other two are the gratings which work with the focal plane instruments to produce high-resolution grating spectrographs. The incoming X-rays reflect from the mirrors to focus on a point, with a width of about half that of a human hair, 30 feet away on the focal plane. ACIS (Advanced CCD Imaging Spectrometer) is a collection of charged coupled devices (CCDs) which measure the energy of each X-rays along with its position. These detectors are the advanced X-ray version of the

⁵<http://www.shuttlepresskit.com/sts-93/payload45.htm>

⁶http://chandra.harvard.edu/about/telescope_system.html

⁷http://chandra.harvard.edu/about/telescope_system.html

⁸<http://www.shuttlepresskit.com/sts-93/payload45.htm>

CCDs in our usual camcorders. Each X-ray liberates tens to hundreds of electrons, depending on its incident energy, which are counted to determine the energy of the X-ray. This gives an energy resolution of 100-200 eV (depending on energy) for the 0.5-8 keV well-calibrated ACIS energy range. Its pixels are read out every 3.2 seconds in normal imaging mode, and are 0.492 arcseconds on the sky. Combining the advantage of energy resolution with its much higher sensitivity (factor >3) above 0.5 keV and much lower background, ACIS is the optimal choice for most Chandra observations. There are two slightly different varieties of CCDs in ACIS; forward-illuminated (FI) and back-illuminated (BI) chips, depending on whether the CCD gates face the incoming X-rays (FI), or not (BI). The FI chips have slightly better energy resolution, background rejection, and sensitivity at high (> 2 keV) energies, while the BI chips have better low-energy sensitivity. There are two ACIS CCD arrays, a 2-by-2 array for imaging of wide fields (ACIS-I, all FI), and a 1-by-6 array (ACIS-S) for use with the diffraction gratings (see below) or imaging of small fields (a BI chip). Each ACIS CCD measures 1024 by 1024 pixels.

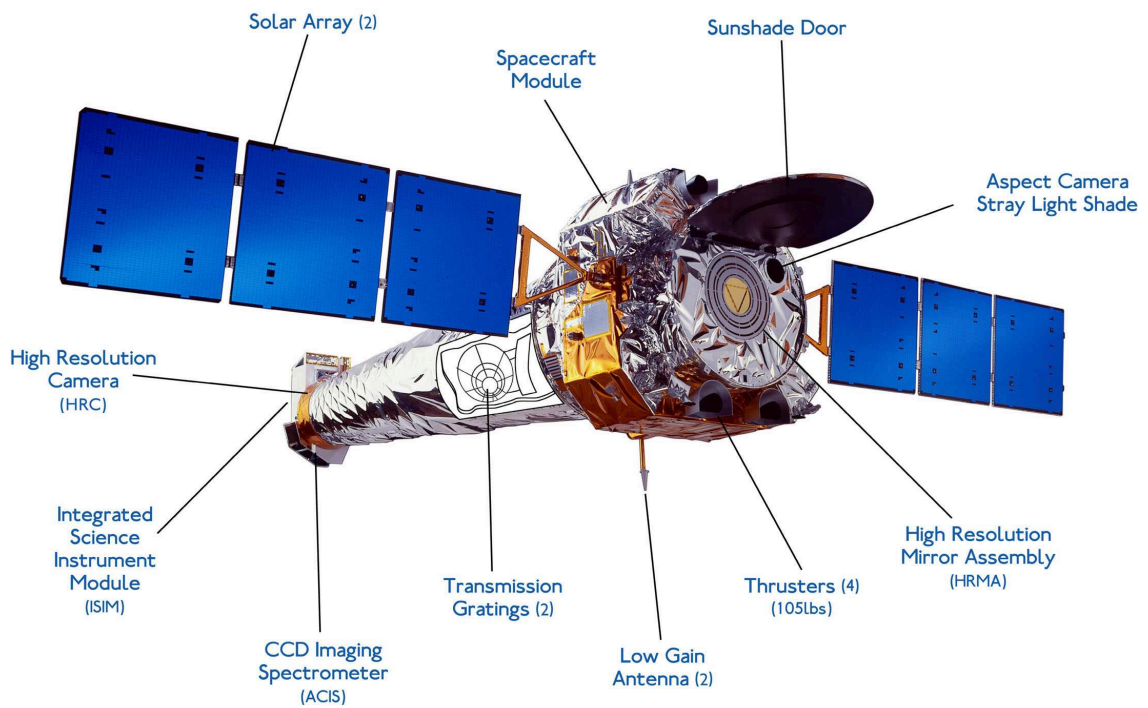


Figure 2.1 Chandra Telescope

This figure shows the different parts of the Chandra telescope.
Credit: NASA/CXC/SAO.

The HRC (High Resolution Camera) provides slightly higher-resolution images due to its smaller pixels, has 16-microsecond time resolution (vs. 3.2 s for ACIS), and has better sensitivity to low-energy X-rays below 0.5 keV.⁹ It uses MCPs (Micro Channel Plates) each composed of a 4-inch square cluster of 69 million lead-oxide glass tubes which are 10 micrometers in diameter and 1 mm long. When the tubes are struck by the X-rays the special coating of the tubes releases electrons which are accelerated down by a high voltage, knocking other electrons out to produce an avalanche of electrons. An electrically charged grid of wires detects the output cloud of electrons and determines the position of the X-ray. There are two HRC detectors, one square for imaging, the other^{10,11} To get more precise spectral measurements of bright sources, one of the two diffraction gratings HETG (High Energy Transmeter Grating) or LETG (Low Energy Transmeter Grating) are placed in the X-ray path between the telescope and the detectors, spreading out the observed spectrum by energy on the detector. These spectrometers have an energy resolution of up to one part in a thousand, allowing identification of discrete X-ray lines for measuring the temperature, ionization and chemical composition of emitting plasma. The LETG grating has an energy range of 0.08-2 keV, and is typically used with the HRC for measurements of low-energy spectra. The HETG has an energy range of 0.4 to 10 keV, and is typically used with ACIS-S for higher-energy spectral measurements. The HRC and ACIS each have two cameras, one square (for imaging) and the other a longer rectangle designed to accomodate diffracted grating spectra. The SIM (Science Instrument Module) is a movable platform on which the focal plane instruments are mounted.

⁹<http://chandra.harvard.edu/about/science/instruments.html>

¹⁰<http://chandra.harvard.edu/about/science/instruments.html>

¹¹<http://www.shuttlepresskit.com/sts-93/payload45.htm>

ACIS FLIGHT FOCAL PLANE

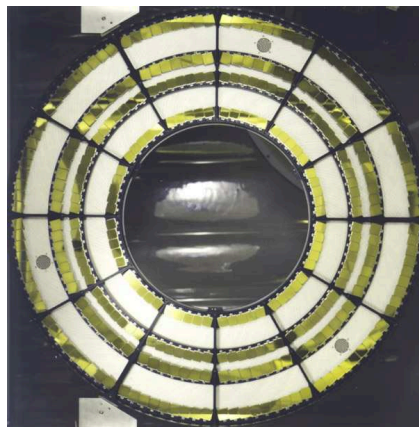
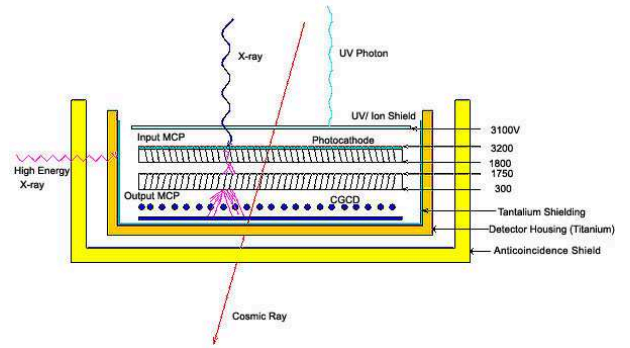
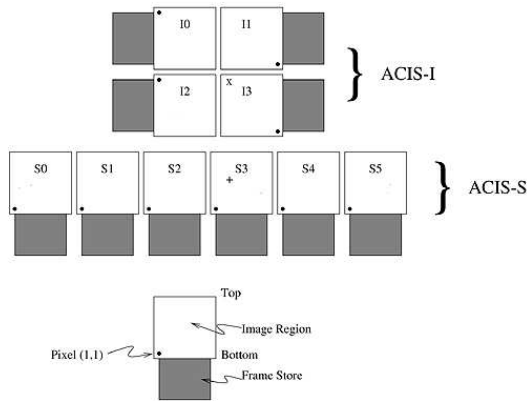


Figure 2.2 The Science Instruments of Chandra Telescope
 On the top left shows the ACIS(Advanced CCD Imaging Spectrometer), top right is HRC(High Resolution Camera) function; on the bottom left is the HETG(High Energy Transmeter Grating), and the bottom right gives a view of LETG(Low Energy Transmeter Grating). Credit:NASA/CXC/SAO.

(c)The Spacecraft: Chandra is supported by the spacecraft to function as an observatory, maintaining its configuration and the environment needed for the telescope. This spacecraft system is consisted of six subsystems: (1) structure and mechanical—all spacecraft structures and mechanisms, including e.g. the “sunshade” door which shadows the telescope aperture from direct sunlight, (2) thermal control—insulation and electrical heaters to keep the mirrors and detectors at constant temperatures, (3) electrical and power—generation of power by two solar array wings, and storage in batteries, (4) communication—including antennas, on-board computer, and telemetry formatter, for receiving commands and sending data, (5) pointing control and aspect determination—responsible for pointing the telescope accurately (using gyroscopes, momentum wheels, and a small optical telescope to track bright stars), solar array control, and safety of the observatory, and (6) integral propulsion—thrusters to control the orbit and spacecraft orientation [Chandra Proposers’ Observatory Guide version 13.0¹²]. Communication with Chandra is via NASA’s Deep Space Network of radio telescopes. Chandra’s operations are controlled by the Operations Control Center in Cambridge, Massachusetts, while the Chandra Science Center (also in Cambridge, Massachusetts) provides data products, calibration, user assistance (especially software), archiving of data, and peer review of observing proposals to produce an observing plan. ¹³.

¹²<http://cxc.harvard.edu/proposer/POG/pdf/MPOG.pdf>

¹³<http://chandra.harvard.edu/about/spacecraft.html>

Chapter 3

X-ray Binaries :

X-ray binaries, as mentioned above, arise from the accretion of gas from a companion star onto a neutron star or black hole. The deep potential well of the compact object brings the accretion disk to extremely high temperatures, producing X-ray radiation. Typically X-ray binaries are divided into two groups, high-mass X-ray binaries and low-mass X-ray binaries, depending on the mass of the companion star.

3.1 High Mass X-ray Binaries(HMXBs):

High mass X-ray binaries have donor stars with masses greater than $5 M_{\odot}$. The donor is usually an O or B type star which emits a dense stellar wind driven by radiation pressure, up to 10^{-6} solar masses per year (compare to 3×10^{-14} solar masses per year in the Sun's solar wind). This stellar wind can be captured by the compact object, producing an X-ray luminosity $L_x \sim 10^{35} - 10^{36}$ erg/s. Four supergiant systems transfer mass by filling the Roche lobe, producing higher L_x up to $\sim 10^{38}$ erg/s [12]. OB-supergiant system containing O or B supergiant stars. Cyg X-1 is an

example, containing an accreting black hole. Be/X-ray binaries contain (typically) main-sequence B stars which are rotating extremely rapidly, and shedding mass at their equator, creating an equatorial “excretion disk” (as they excrete, rather than accrete, this gas). The “e” in “Be” refers to the emission lines seen in their spectra, produced by this equatorial disk of hot gas. Be X-ray binaries are typically transients, dramatically rising in luminosity when the neutron star passes through the equatorial disk of the donor star [12].

The neutron stars in high-mass X-ray binaries are relatively young (compared to the neutron stars in low-mass binaries, below), and retain the strong magnetic fields they were born with (typically 10^{12} G). The magnetic field pressure is strong enough to channel the material in the accretion disk onto the magnetic field lines, and thus it accretes onto the magnetic poles of the neutron star. As the neutron star rotates, the poles rotate into and out of our line of sight, producing pulsations at the neutron star spin frequency; these systems are thus X-ray pulsars. [7]

In our Milky way there are ~ 300 HMXBs [13, 14]. Most have large orbital separations and relatively long periods ($\sim 1 - 100days$), and are known or thought to contain neutron stars. The donor O or B stars have short life times $\tau_{donor} \sim 100$ Myr [15], so HMXBs are seen only in regions of recent star formation. The Small Magellanic Cloud has undergone a recent burst of star formation, and shows a very high abundance of high-mass X-ray binaries, principally Be X-ray binaries, of which 60 are identified so far [16].

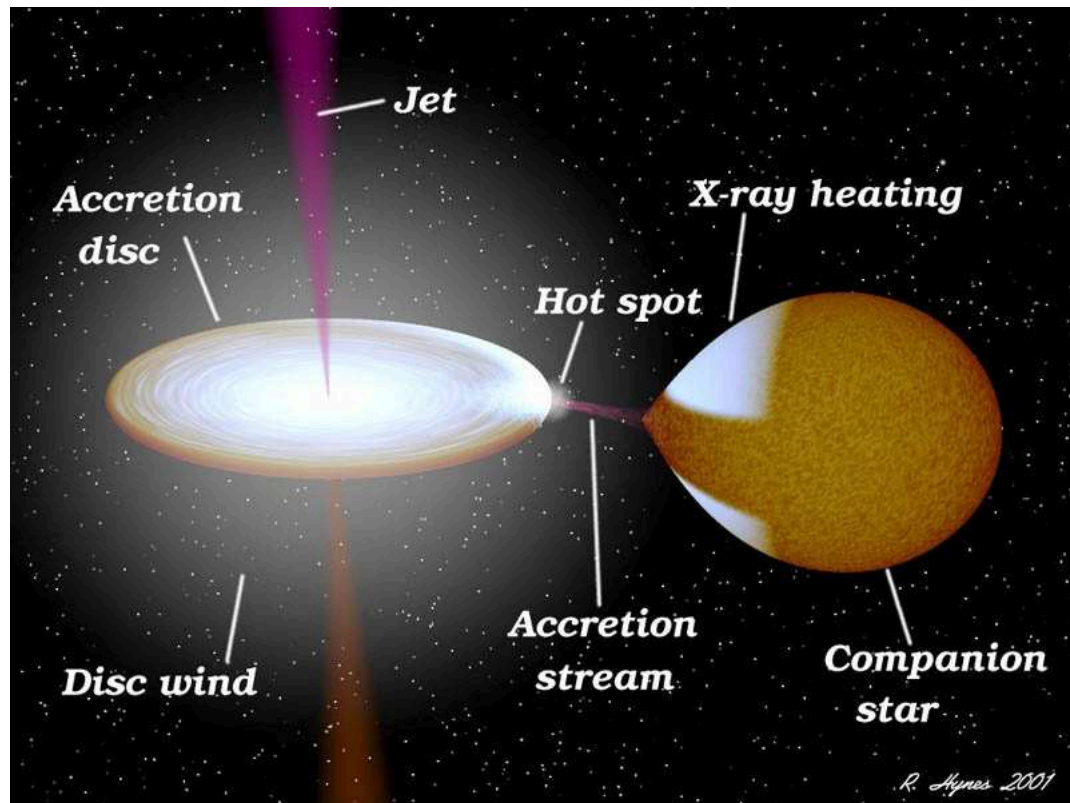


Figure 3.1 X-ray Binary System

XRB is a binary stars system which are very luminous in X-rays. The matter falling from the companion star to the compact one produces the X-ray emission. This fig. shows an illustration of an X-ray binary star system. Credits: NASA /R. Hynes.

3.2 Low Mass X-ray Binaries(LMXBs):

In the LMXB case the donor star mass is low, $M_{don} \leq 2M_{\odot}$, typically K or M stars [7]. Since the donor star must fill its Roche lobe, they have short orbital periods ranging $10min - 10days$, with a median of $\sim 9hours$ [14]. Their long lifetimes ($\tau_{don} \sim 1-10$ Gyr) approach the lifetime of the universe for $M_{don} \leq 0.8M_{\odot}$. Most LMXBs accrete materials through Roche-lobe overflow, as stellar winds from low-mass main sequence stars are weak, though some LMXBs have giant donors with high mass-loss rates and long periods. The long lifetime of LMXBs means that they are found in stellar populations of all ages, including in old elliptical galaxies with no high-mass stars.

LMXB formation requires a low-probability event, causing them to be rather rare considering their lifetimes. The neutron star (or black hole) is formed in a supernova explosion that disrupts a high-mass star ($> 10M_{\odot}$). Since the system that remains contains a low-mass ($< 2M_{\odot}$) star, and a $< 2M_{\odot}$ neutron star, more than half of the total mass of the binary is lost in the supernova. This is sufficient to unbind the binary, so if this were the whole story no LMXBs should exist. However, neutron stars (and probably black holes) receive an additional velocity “kick” in the supernova explosion averaging 400 km/s, whose origin is unclear [17]. In some binaries, the kick happens to be of the correct magnitude and direction to leave the neutron star in orbit around the low-mass star, allowing future evolution to bring the stars together.

It is observed that very few neutron stars in LMXBs show X-ray pulsations, suggesting that the magnetic field does not control accretion. Neutron stars in LMXBs often show “X-ray bursts”, rapid thermonuclear burning of accreted light elements on the neutron star surface. These bursts cannot take place in the presence of a strong magnetic field. The lack of pulsations, and presence of bursts, suggests magnetic field

strengths of $B \sim 10^{8-9}$ G in LMXBs. As LMXB accretion can continue for billions of years, a substantial amount of material can be transferred onto the neutron star. This accreted material may “bury” the magnetic field of the neutron star, reducing the observed magnetic field to the weaker observed value [18].

3.3 Accretion Disks:

Material in the accretion disk, in order to spiral down to the accretor star, must lose angular momentum and energy. Losing energy can be accomplished through radiation, but angular momentum must be transferred from one particle to another, so the disk must spread out in order for matter to accrete. This requires transfer of angular momentum between particles, which requires viscosity in the material. The principal source of this viscosity is now thought to be a magneto-rotational instability—weak magnetic fields in a disk containing charged particles are strengthened by the differential rotation of the disk, producing interactions between particles [19]. Thus, the disk should have much higher viscosity when it is (at least partly) ionized (at high temperatures, above ~ 6000 K to begin ionizing H), than when it is not ionized (at lower temperatures). A disk begins in a relatively cold state, and as it accumulates a substantial amount of mass the pressure and temperature in its densest parts increase, until it heats up enough to increase its viscosity. Once a disk reaches a high temperature and begins to flow, the release of potential energy as radiation heats the disk further, ensuring it stays in a hot, viscous state until most of the disk has accreted onto the central object [20].

3.4 Transient Behavior:

The disk instability model above suggests two classes of accreting binaries. Those where the transfer of material from the donor is at a high enough rate to continuously keep the disk in a hot state give stable mass transfer, leading to persistently accreting binaries. If the mass transfer rate is lower, the available material in the disk can be exhausted, accretion stops, and a cold disk starts building up again.

Both CVs and X-ray binaries are indeed divided into two classes—those with persistent mass transfer (generally at higher mass transfer rates) and those that show transient behavior. Nearby CVs show this behavior most clearly in the optical, where “novalike” systems are persistently bright, while “dwarf nova” systems show transient brightenings by several magnitudes. Transient X-ray binaries show periods when they are ‘turned off’ in X-rays, so-called quiescent episodes where $L_X \leq 10^{33}$ ergs/s, for long periods of time (from months to at least decades). They ‘turn on’ for ‘outbursts’ of X-ray luminosity $> 10^{36}$ ergs/s (typically > 1000 times their quiescent luminosity), often lasting 10-100 days [21]. X-ray binaries are expected to have different transient behavior than CVs, since the energy released in accretion is substantially greater and the resulting X-ray irradiation can prolong their outburst state.

The majority of X-ray binaries are transients, and the larger part of these have only been carefully studied during outburst. Galactic X-ray binaries in outburst can typically be detected by all-sky X-ray monitors, such as that on the Rossi X-ray Timing Explorer. However, many X-ray binaries have only been seen in outburst once, so the details of their transient behavior (recurrence time, fraction of time in outburst) are not known.

3.5 LMXBs In Quiescence:

X-ray binaries in quiescence were first identified based on the positional coincidence of a bright transient’s location [22], though now they can often be identified based on their typical X-ray spectrum [23,24]. X-ray binaries in quiescence show different behavior depending on the nature of the accretor; neutron stars show much brighter X-ray emission than black holes, with a particularly “soft” (low-energy) spectral shape. A tiny amount of accretion seems to continue in quiescence, providing faint ($L_X < 10^{32}$ ergs/s) X-ray emission from both black holes and neutron stars. The neutron stars show an additional soft component, with the shape of a blackbody spectrum, while the hard spectral component from both neutron stars and black holes is usually fit with a power-law energy spectrum of photon index 1-2 [21].

The blackbody-like X-ray emission of neutron stars in quiescence is thought to be due to re-radiation of heat from the core of the neutron star, produced in the inner neutron star crust during the time of outbursts [26]. The spectrum emerging from a typical quiescent neutron star X-ray binary will be altered by passing through the dense, ionized atmosphere. This atmosphere is presumably hydrogen if hydrogen is among the accreted elements, since the atmosphere stratifies within a minute, with the lightest elements rising to the top. Model hydrogen atmospheres constructed for neutron stars with low magnetic fields (as seen in LMXBs) resemble blackbody spectra, but the frequency-dependent opacity of the atmosphere shifts the spectra to higher energies [27]. Fitting these models to the spectra of observed transient LMXBs in quiescence gives good fits, and the inferred sizes of the emitting object are consistent with standard (e.g. ~ 10 km radius) neutron stars.

In this work we use the NSATMOS hydrogen-atmosphere neutron star model

[28,29]. It has four key parameters- M_{ns} (the neutron star mass in the unit of M_{\odot}), R_{ns} (the true radius of the NS in kms), T_{eff} (the unredshifted effective temperature of the surface of NS), and D (the distance to the NS in pcs). This model was designed to self-consistently model the surface gravity for the chosen NS mass and radius, and also incorporates electron thermal conduction, radiation force, and self-irradiation of the neutron star. For the appropriate surface gravity range it agrees well with the model of Zavlin et al. (1996) [27].

3.6 Populations Of Bright XRBs In Our Galaxy:

Grimm, Gilfanov & Sunyaev (2002) [30] used the All-Sky Monitor on the RXTE satellite to study the spatial and luminosity distributions of bright XRBs in our Galaxy. If we consider the spatial (3-D) distribution of XRBs in the Milky Way, we notice the HMXBs are crowded in the Galactic Plane with a vertical scale height of 150 pc while the LMXBs are concentrated in the Galactic Bulge, and to a lesser extent in the Galactic plane and halo [30]. Their spatial distributions are consistent with the paradigm that HMXBs occur in regions of recent star formation, while LMXBs are distributed similarly to stellar mass (with the exception of globular clusters, see section 3.7).

A variety of methods have been used to estimate distances to bright XRBs, summarized by Grimm et al.(2002) [30] Distances have not been estimated to all XRBs, and existing distance estimates are imperfect, so luminosity estimates are somewhat uncertain. The highest-flux objects are smallest in number and best-studied, so their luminosities are the most well-determined. Persistent systems above $L_X(2-10 \text{ keV}) > 10^{36}$ ergs/s can be detected throughout the Galaxy (if they are not hidden

by dense gas or proximity to other sources), so a decent estimate can be made of their numbers, approximately 100 LMXBs above 10^{36} ergs/s in the Galaxy. Extrapolating below this is more uncertain; Grimm et al. [30] estimate ~ 325 LMXBs with $L_X > 10^{34}$ ergs/s, but this is uncertain to within a factor of two. The distribution of LMXBs and HMXBs in our galaxy is shown in the Fig.3.2 below:

3.7 The Total Number Of LMXBs, qLMXBs, And Duty Cycles:

Estimation of the total number of LMXBs in the Galaxy would require accounting for the total numbers of LMXBs in quiescence. The most straightforward approach would be to directly identify quiescent LMXBs in a portion of the Galaxy. However, this task is extremely difficult due to their X-ray faintness, putting them in or near the same L_X range as large numbers of other sources (e.g. CVs, and chromospherically active binaries; see sections 3.3, 3.5), and their optical faintness, which makes typical LMXBs extremely difficult to identify at typical distances of the Galactic bulge. The unusually soft X-ray spectra of quiescent neutron star LMXBs could offer a method for identification of quiescent LMXBs, but most LMXBs are observed in or near the Galactic plane, where soft X-rays are absorbed by the gas and dust of our Galaxy's interstellar medium (for instance, the absorbing column of gas towards the Galactic center, 6×10^{22} atoms cm^{-2} , removes most photons below 2 keV and all photons below 1 keV). Full-sky surveys to identify the few quiescent LMXBs within 1000 pc of Earth could overcome the absorption problem, but the spectral and angular resolution of existing surveys is relatively poor.

Another approach is to estimate the number of quiescent LMXBs using the measured number of bright LMXBs, and an estimate of their duty cycle. The duty cycle is defined as the fraction of the time when LMXBs are in their 'on' stage, in outburst. For transient sources with time in quiescence ($T_{quiescence}$) and in outburst ($T_{outburst}$), the duty cycle can be given as:

$$DC \equiv T_{outburst} / (T_{outburst} + T_{quiescence}).$$

The thermal disk instability model [32–35] is not well-enough understood to explain the values of luminosity of the outburst, or to allow direct calculation of the duty cycle [102]. The time period for the outbursts observed in our galaxy and nearby galaxies for several transient LMXBs [36] is usually in the scale of months while the duration for quiescence stages between the outbursts, in general, spend one to few years resulting in an estimated duty cycle of 1-10 % [100]. However, this is based on a limited number of selected systems, which have outbursts bright and long enough to be detectable (vs. short, dim outbursts, e.g. 6440 X-2 [56]), but not so long (decades) that they have only been seen in outburst. As the outburst length is thought to be correlated with the orbital period, this estimate of duty cycle may be appropriate only for systems of medium-length orbital periods (few hours to a day), where the donor is a main-sequence star with mass $\sim 0.3 - 1 M_{\odot}$.

An alternative estimate for the duty cycle of neutron star systems comes from measuring the heat deposited in the core of neutron stars during outbursts, and re-radiated away in quiescence [26]. Since the timescale for heat to emerge from the core is $> 10^4$ years, the quiescent emission can be compared with the heating rate, averaged over many outbursts and quiescent periods. The neutron star LMXB KS 1731-260 had been accreting for 12.5 years when it turned off in early 2001. Wijnands et al. (2001) [37] observed KS 1731-260 in quiescence with Chandra, finding its quiescent

X-ray luminosity to be $L_X(0.5-10 \text{ keV}) \sim 1 \times 10^{33} \text{ ergs/s}$. If the heat deposited during outburst is all radiated away as photons during quiescence, a quiescent timescale of at least 200 years is required, and a duty cycle of $<5\%$. More recent observations have observed continued cooling, by another factor of 7 [48], suggesting a quiescent timescale of >1400 years and a duty cycle $<1\%$. However, the heat may be radiated away through neutrino emission from the core through fast cooling processes, as indicated for some LMXBs with measured quiescent fluxes and known outburst recurrence times such as Cen X-4 [104] and SAX J1808.4-3658 [49, 50]. This possibility makes quiescent luminosity measurements unreliable for duty cycle estimates.

A third estimate comes from detailed simulations of the disk instability for particular systems, using smoothed particle hydrodynamics (SPH) simulations. Deegan et al. calculate the duty cycle for their model of the long-period (33.5 days) LMXB GRS 1915+105, which has been in outburst continuously since 1992. For such a system, with a giant star as a donor, the accretion disk is large, producing long outburst and quiescent times. Deegan et al. [100] estimate the quiescent and outburst timescales to be 20-130 years and 7000-20000 years respectively, implying a duty cycle for GRS 1915+105 of $\sim 0.1-0.5\%$. Uncertainties in this approach include which physical mechanisms must be considered in the analysis, and how to extrapolate from modeling individual systems to a (poorly-constrained) population.

3.8 Globular Cluster XRBs:

The stellar densities, excluding some galactic nuclei, are quite low for most parts of galaxies. For instance, the local mass density near the sun is $\sim 0.1 M_\odot \text{ pc}^{-3}$ [38]. About 147 GCs are distributed spheroidally around our Galaxy's center [1]. GCs are

spheroidal shaped clusters of up to millions of stars, with often much higher stellar densities, up to $10^5 - 10^6$ stars in a diameter of 10 pc to 30 pc [2]. In their dense cores the stellar densities can reach 10^6 stars pc^{-3} . At these high densities stellar interactions are very likely to occur, which can create or destroy binaries.

As these clusters are old, all normal stars with masses larger than the Sun will have evolved through the giant stage to produce stellar remnants. These dynamical interactions are of interest since they can place stellar remnants, which are often the most massive objects in the cluster, into new binary systems, giving an increased chance of forming LMXBs. Binaries with stellar remnants may form in GCs through physical collisions, or exchange interactions involving a pre-existing binary and another star which replaces one of the original binary members [40]. Such exchanges are most likely to leave the heaviest of the three stars in the binary—which favors placing stellar remnants into binaries. As LMXBs are difficult to form (see section 3.1), these mechanisms are particularly important in producing LMXBs in GCs. The number of bright LMXBs per unit stellar mass is indeed much higher (~ 100 times more common) in GCs than the rest of the Galaxy [41, 42].

Among 12 GCs fifteen bright LMXBs are recognized with at least eight of them showing 'outburst' episodes of their transient behaviour and longer quiescent times [51, 56, 58]. Most of the bright X-ray sources ($L_x > 10^{36}$ ergs s^{-1}) in GCs are NS LMXBs [52, 53]. The X-ray luminosity function (ratios of the number of sources per luminosity bin) appears similar for globular clusters and other old stellar populations, such as elliptical galaxies [51, 60, 62]. However, a large fraction (at least 6 of 15) of LMXBs in GCs are "ultra-compact" systems (periods less than one hour), indicating that the donor star is hydrogen-poor (most likely a white dwarf) [63–65]. Such systems are easily formed in globular clusters through the collision of NSs with red giants [66],

but are much rarer in the rest of the Galaxy [47]. Therefore it is not clear that conclusions derived from GC LMXBs may be applicable to LMXBs in the rest of the Galaxy.

The population of low- L_X X-ray sources ($L_X \leq 10^{34}$ ergs s^{-1}) in GCs includes LMXBs containing transient NSs in quiescence [43], CVs [67, 68], millisecond radio pulsars [24, 69] and chromospherically active binaries [24, 25]. Hundreds of low- L_X X-ray sources have now been identified in dozens of globular clusters using the small point-spread function and good sensitivity of Chandra [103], and in many cases their optical counterparts have been identified using Hubble Space Telescope imaging [25]. Quiescent LMXBs can (often) be separated from the other sources by their combination of L_X and soft spectra [23, 24, 44], which has allowed the identification of a large population of dozens of quiescent LMXBs in GCs [46]. These quiescent LMXBs are dominated by their soft X-ray spectra, with L_X between 10^{32} and 2×10^{33} ergs/s. However, the faintest LMXBs in quiescence tend not to be dominated by their soft spectral components [57]. This indicates that a similar-sized population of quiescent LMXBs probably lies unidentified among the faint sources with harder spectra; a deep X-ray observation of the GC 47 Tucanae identified three quiescent LMXBs among this population [54].

It is possible to use the observed structure of globular clusters (specifically, their central stellar density and core size) to predict the relative stellar interaction rates between different clusters; this reasonably predicts the clusters in which bright LMXBs are most likely to be found [101]. A similar correlation between predicted interaction rates and the numbers of low- L_X X-ray sources has been observed [59], indicating that many of these are also formed through stellar interactions. Using this correlation to extrapolate from the GCs that have been studied with Chandra, some 200 quiescent

LMXBs have been estimated to exist among the Galactic GCs [54]. Considering that about 10 LMXBs are observable among Galactic GCs in any year, this suggests an LMXB duty cycle of $\sim 5\%$. However, since GC LMXBs are rather different from Galactic LMXBs, it's unclear that this duty cycle can be applied to Galactic LMXBs.

3.9 LMXBs In Other Galaxies:

Many other galaxies have been studied with current X-ray instruments, down to the L_X limits of 10^{35} ergs/s in M31 (Andromeda galaxy, [55]). These observations can identify large numbers of bright LMXBs, but are unable to penetrate to the quiescent LMXB population. However, recent deep observations of the nearest dwarf galaxies, the Sculptor Dwarf and the Small Magellanic Cloud, reach L_X limits below 10^{33} ergs/s, and thus present the possibility of identifying quiescent LMXBs. The detection of quiescent LMXBs has been claimed in the Sculptor Dwarf by Maccarone et al. (2005) [61], on the basis of five X-ray sources with $L_X > 6 \times 10^{33}$ ergs/s, associated with giant stars as counterparts. These systems, however, do not resemble typical quiescent NS LMXBs in luminosity or spectra. Maccarone et al. suggested that these systems are long-period LMXBs in quiescence, which would indicate a very large population of quiescent long-period LMXBs in low-density populations (such long-period binaries would likely be destroyed in dense globular clusters through stellar interactions). Heinke et al. (2011) [70] instead suggest that Maccarone et al.'s X-ray sources are symbiotic systems—meaning that the X-rays are generated by wind accretion rather than Roche lobe overflow, and that these systems are radiating at their average flux level (no bright outbursts occur).

The focus of this thesis is to attempt to estimate the total number of quiescent

LMXBs, and thus average duty cycle, in an external galaxy. Choosing an external galaxy removes the problem of dust and gas obscuring soft X-rays from quiescent NS LMXBs, allowing identification of quiescent LMXB candidates by their soft X-ray spectra. We use deep Chandra observations of two fields in the Small Magellanic Cloud (SMC) to search for these systems.

3.10 Known XRBs In The Magellanic Clouds:

The SMC is a star-forming dwarf galaxy and satellite galaxy of the Milky Way $\sim 63kpc$ away from us. It has been well-studied due to its nearby location and recent star formation, characterized by roughly 1/2 of the stars being older than 8 Gyrs, and the other half forming in bursts 2.5, 0.4, and 0.06 Gyrs ago [71]. Its foreground (Galactic) extinction is relatively low, $N_H \sim 6 \times 10^{20} \text{ cm}^{-2}$, though molecular clouds within the SMC obscure some sources.

The SMC's recent star formation history has produced a quite substantial overabundance of Be X-ray binaries compared to the Galaxy, with a similar number of Be XRBs known in the SMC as in the Galaxy despite a factor of 50 difference in their masses [72, 73]. This is probably due to Be XRBs generating their excretion disks (see section 3.1) at ages of 25-80 million years [74], consistent with the age of the most recent burst of star formation in the SMC. Some 92 HMXBs and HMXB candidates are known in the SMC, with 50 confirmed Be XRBs and only one supergiant HMXB (Antoniou et al. 2009). No bright LMXBs are known in the SMC, but this is consistent with its small mass relative to the Milky Way which would only predict 1-2 LMXBs; the more massive Large Magellanic Cloud (LMC) has two known LMXBs [36].

The Be XRBs are transient sources, which motivated the deep Chandra surveys of the SMC to detect them in relative quiescence. Laycock et al. (2010) [75] identified fifteen HMXBs (and three candidate HMXBs) in quiescence in these deep fields, most showing clear pulsations, with $L_X \sim 5 \times 10^{32}$ to 5×10^{35} ergs/s, and hard X-ray spectra (fit by power-law spectra $F_\nu \propto \nu^{-0.3}$). The hard X-ray spectra of HMXBs in quiescence is relatively common [77], and helps to separate quiescent HMXBs from quiescent LMXBs.

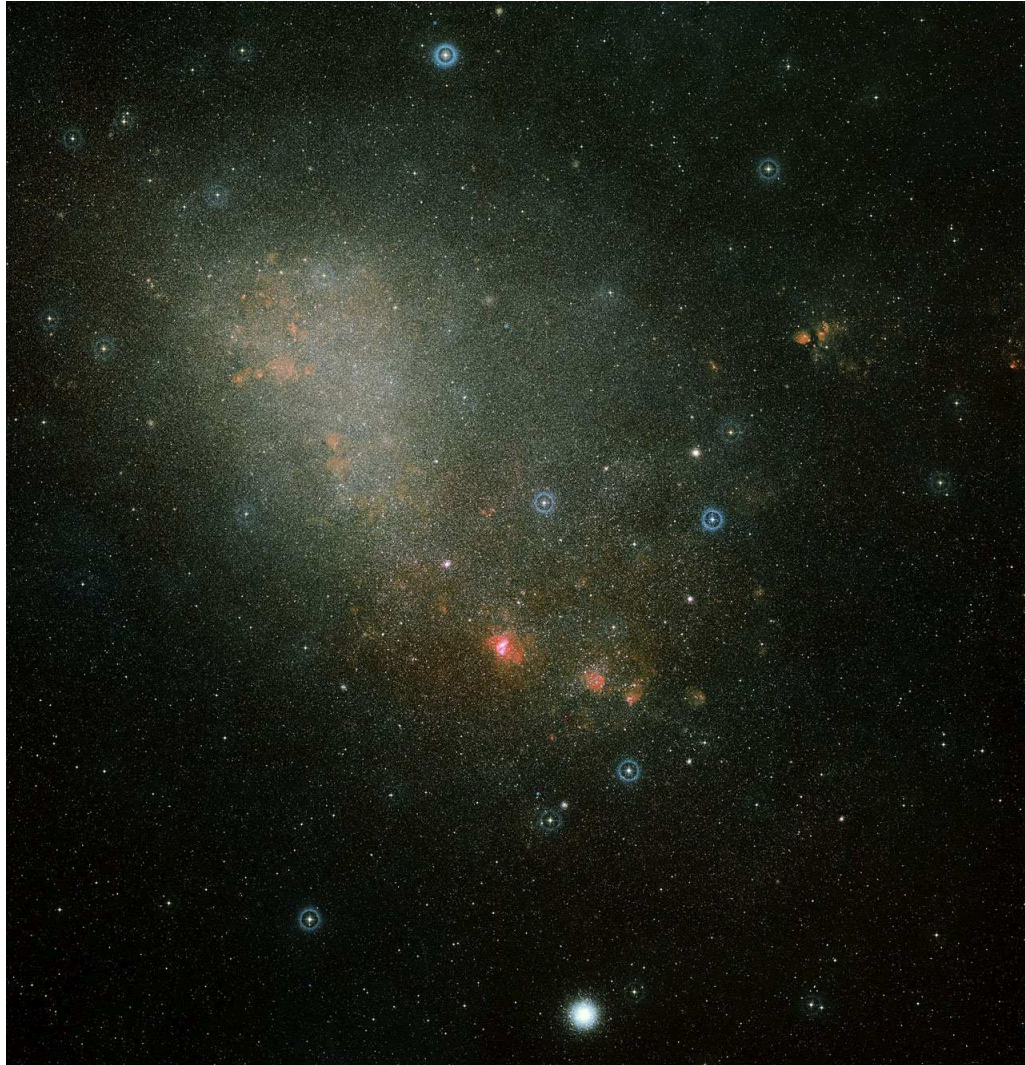


Figure 3.2 Small Magellanic Cloud

The two-colour image shows an overview of the full Small Magellanic Cloud (SMC). Credit: ESA/Hubble and Digitized Sky Survey 2. Acknowledgements: Davide De Martin (ESA/Hubble) .

Chapter 4

X-ray Analysis:

4.1 The Chandra Deep Fields Of The SMC:

The two Deep fields in SMC are positioned at the most active star forming zone of the bar ($\sim 4.4\%$ of SMC). The Deep Field 1 (DF1) is located in a very pulsar dense region [80]. RXTE has monitored the SMC, often pointing near DF1 [76] while Deep Field 2 (DF2) was first observed by Chandra in 2002 [79], as part of five short observations in the central part of the SMC [73]. Lengthy observations of 100 ksec were then performed by Chandra on the two SMC Deep Fields [80]. We downloaded data on DF1 & DF2 of the SMC from the Chandra X-ray Observatory's public archive. The Advanced CCD Imaging Spectrometry (ACIS) was used, with the ACIS-I array at the focus of the telescope. DF1 was observed in two observations over the course of two days. DF2 observation was divided into three observations over a single day. Focus-points were identical for each field's observations making it easier for data reduction. The table 4.1 shows the details of the DF1 & DF2 observations:

Table 4.1. **Observations**

Obs. ID	Object	RA	DEC	Obs. Date	Exp. Time(ks)
7155	SMC DF1	13.39375	-72.445333	2006-04-26	49.31
7156	SMC DF2	12.6725	-73.269528	2006-11-24	386.27
7327	SMC DF1	13.39375	-72.445333	2006-04-28	47.39
8479	SMC DF2	12.6725	-73.269528	2006-11-24	42.09
8481	SMC DF2	12.6725	-73.269528	2006-11-24	15.97

4.2 Data Reprocessing And Background Removal:

We used the CIAO version 4.1¹ to reduce the data. A new bad pixel file was created using the `acis_run_hotpix` script. We reprocessed the level = 1 event files using new calibrations for charge-transfer efficiency on the detector and time-dependent gain adjustments. Using the standard CIAO Science Threads², all standard Chandra calibration and corrections as exposure-map corrections, cosmic ray afterglow removal and filtering data on grade and status to create level = 2 event files are done.

¹<http://cxc.harvard.edu/ciao4.1/download/>

²<http://cxc.harvard.edu/ciao4.1/threads/all.html>

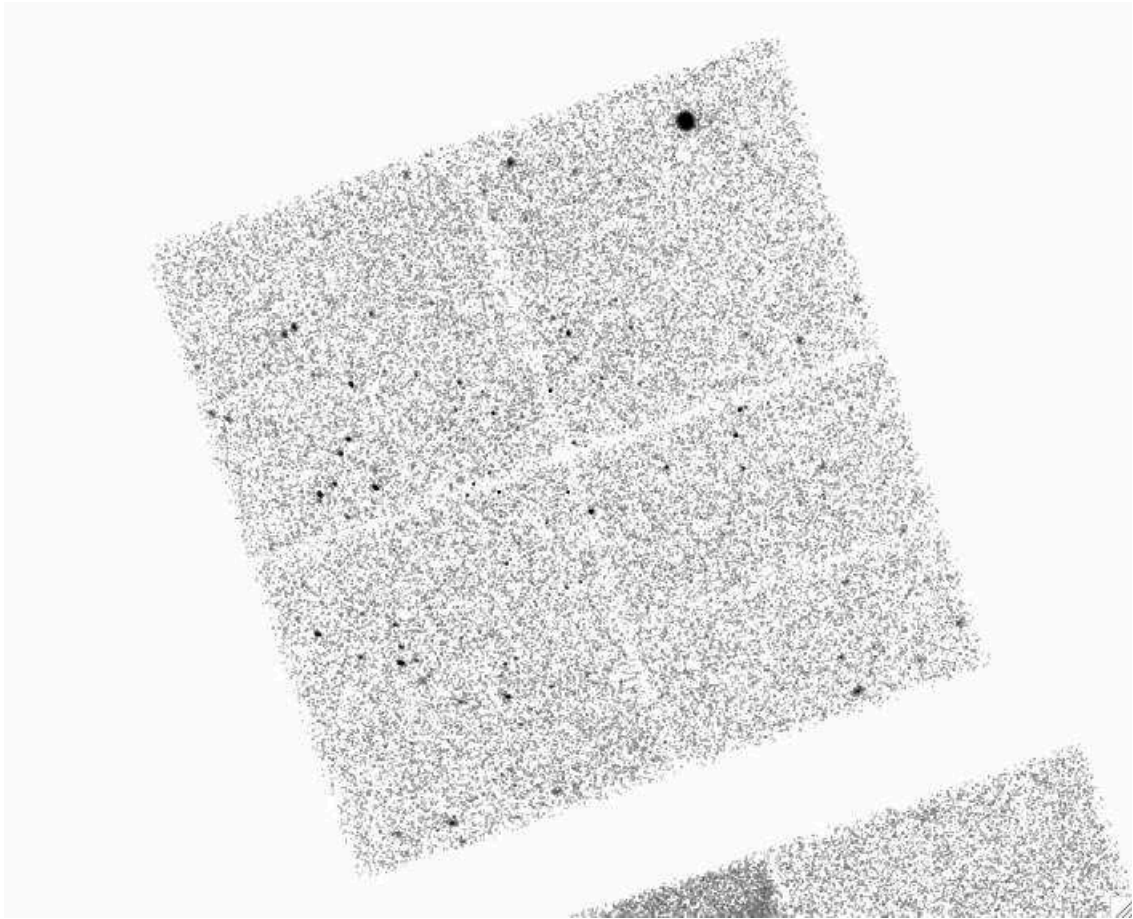


Figure 4.1 Image of DF1 Chandra Data
North is up, East to the left. $16' \times 16'$ is measured on each side of the field by ACIS-I. The brightest source is a Pulsar SXP326.

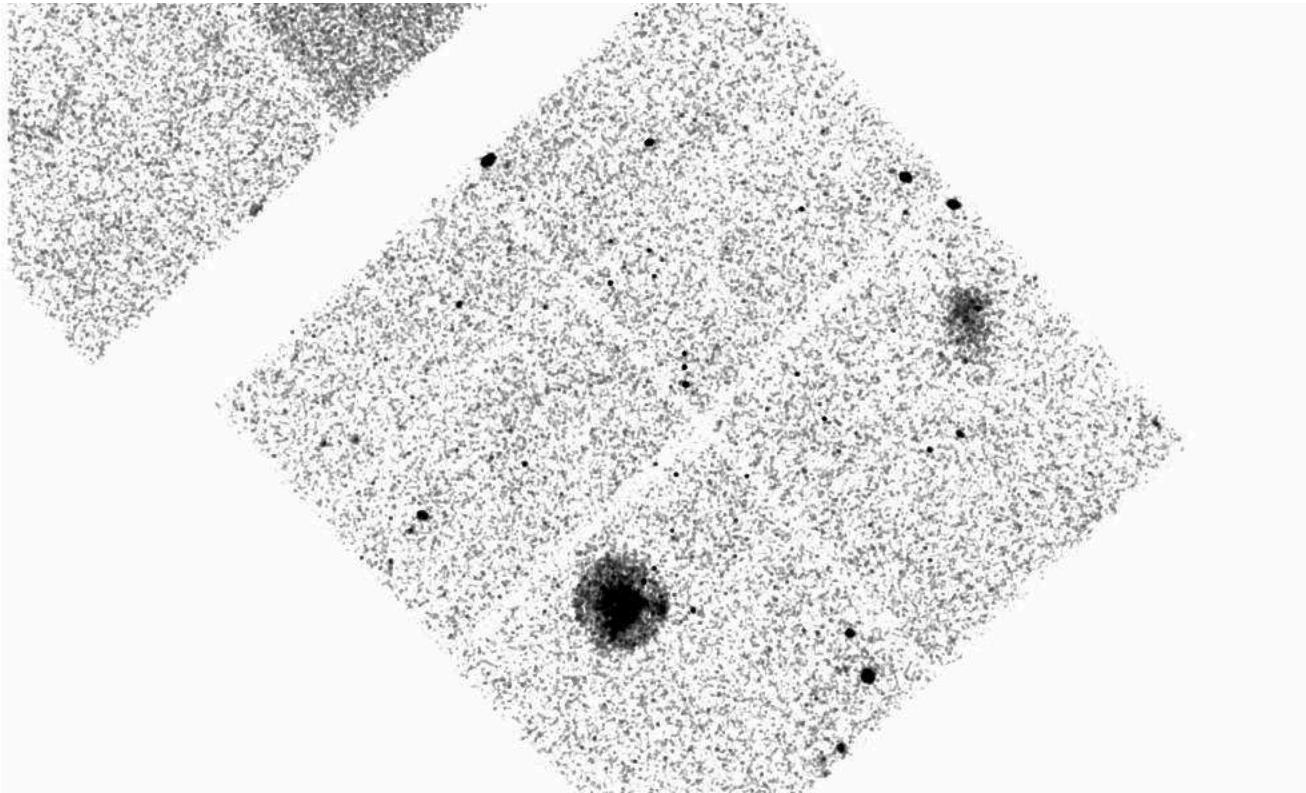


Figure 4.2 Image of DF2 Chandra data
North is up, East to the left. $16' \times 16'$ is measured on each side of the field by ACIS-I. The brightest object a Supernova remnant, there is also other supernova remnant located to the upper right as a much fainter source than the other.

4.3 Source Detection:

The wavelet detection algorithm(CIAO *wavedetect* program) is used to find out the discrete XRS populations on the ACIS-I images of the two Deep Fields in the SMC and to get the confirmation a local cell detection method and visual inspection is made. We set the probability of wavelet source detection threshold to 10^{-6} that assured ≤ 1 false source detection possibility in the whole ACIS-I image. We search the sources in the energy limit of 0.3 - 7.0 keV to detect all sources both in soft band and in hard band. We have used the wavelet scales 2 and 4 pixels(1 pixel = 0.492"). We found 226 sources in DF1 and 212 in DF2.

4.4 ACIS_EXTRACT Data Extraction:

The IDL program ACIS_EXTRACT(AE)³ was used for extracting source photometry and spectra and improving the source positions(Feigelson et al. 2002).We used the step by step strategy to improve the position of sources to make quality source catalogue for the both Deep Fields.The flowchart of fig. 4.3 shows the major steps of our AE works [78].

³http://www.astro.psu.edu/xray/docs/TARA/ae_guide.html

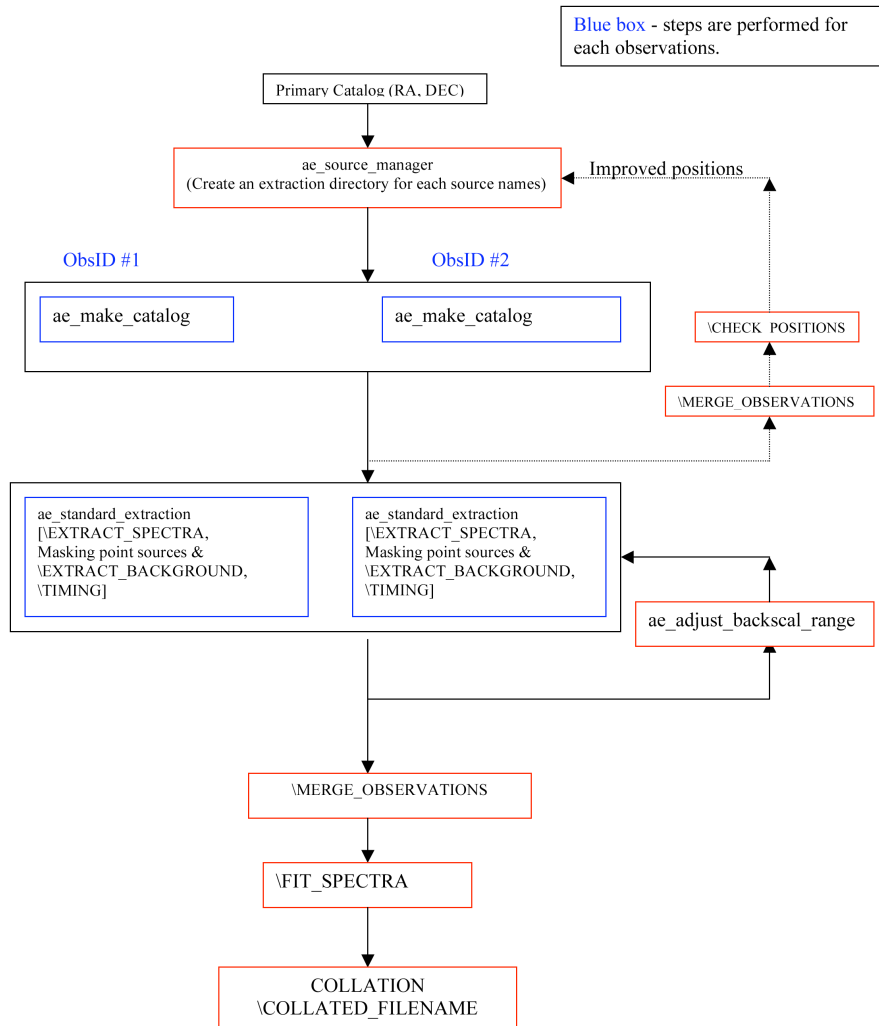


Figure 4.3 Overview of the AE steps

We start with the sources detected by the wavedetect as our primary catalog.

1. ae_source_manager tool is used to create an extraction directories for each sources and to keep a file with the list of the source names.
2. ae_make_catalog do the job of constructing non-overlapping extraction regions for each ObsIds(Observation IDs) that known as the step of CONSTRUCT_REGIONS. In this stage source names are made up and the celestial coordinates provided and source extraction directories are made.PSF(Probability Spread Function) images for all sources are constructed on this step.
- 3.Review of the catalog constructed are done by CHECK_POSITIONS stage to add new sources or delete sources.
4. ae_standard_extraction is a very efficient step to perform spectral extraction and extraction of background spectra from each source in each ObsId.Timing stage is also performed by this tool by constructing light curves for each ObsIds.
- 5.ae_adjust_backscal_range is used to scaling the target background and this step is repeated as needed.
- 6.MERGE_OBSERVATIONS stage is for combining the single ObsIds and producing multi-ObsID spectra.
- 7.FIT_SPECTRA is used for deriving spectral models from multi-ObsId spectra for using in the spectral analysis of the XSPEC scripts for AE ⁴.
- 8.COLLATION step collates all data products, and includes chosen spectral model of the observer in a big FITS table.

After the extraction stages were succesfully execuated we got two catalogs one with 68 sources in DF1 and another with 50 sources in DF2. The Table 4.2-4.4 and Table 4.5-4.6 shows the detailes of the extracted sources from DF1 & DF 2 with their

⁴cp -R /usr/common/rsi/lib/apps/TARA/code/ae/xspec_scripts

Table 4.2. Luminosities and Counts of the DF1 XRSs

Src. ID	L_x (0.5-7.0) keV	L_x (0.5-2.0) keV	L_x (2.0-7.0) keV	cnts (0.5-7.0) keV	cnts (0.5-2.0) keV	cnts (2.0-7.0) keV
005153.41-723149.0	1.217e+34	3.486e+33	8.690e+33	189 ^{+14.77} _{-13.73}	79 ^{+9.93} _{-8.87}	112 ^{+11.618} _{-10.56}
005205.65-722604.2	5.421e+33	2.022e+33	3.231e+33	78 ^{+9.84} _{-8.81}	38 ^{+7.22} _{-6.14}	41 ^{+7.46} _{-6.375}
005231.80-722434.3	1.370e+33	8.909e+32	3.018e+32	18 ^{+5.33} _{-4.2}	13 ^{+4.7} _{-3.56}	5 ^{+3.39} _{-2.16}
005232.28-722607.7	1.450e+33	9.801e+32	2.695e+32	32 ^{+6.72} _{-5.63}	26 ^{+6.17} _{-5.07}	6 ^{+3.59} _{-2.38}
005233.69-722437.6	7.133e+33	1.889e+33	5.297e+33	115 ^{+11.75} _{-10.71}	44 ^{+7.68} _{-6.61}	72 ^{+9.52} _{-8.42}
005235.07-722516.5	7.660e+33	3.519e+33	3.668e+33	122 ^{+12.07} _{-11.03}	68 ^{+9.29} _{-8.23}	55 ^{+8.46} _{-7.4}
005237.35-722732.6	4.834e+32	3.067e+32	1.167e+32	12 ^{+4.57} _{-3.41}	8 ^{+3.95} _{-2.77}	4 ^{+3.17} _{-1.91}
005245.25-722844.0	9.500e+32	6.951e+31	9.526e+32	12 ^{+4.57} _{-3.42}	4 ^{+3.17} _{-1.91}	8 ^{+3.95} _{-2.77}
005250.28-722902.2	1.070e+33	4.233e+32	6.053e+32	19 ^{+5.44} _{-4.32}	9 ^{+4.12} _{-2.94}	10 ^{+4.27} _{-3.11}
005252.25-721715.7	6.765e+35	2.282e+35	4.360e+35	8426 ^{+92.79} _{-91.79}	3749 ^{+62.23} _{-61.23}	4699 ^{+69.55} _{-68.55}
005258.44-722606.7	5.426e+33	1.607e+33	3.799e+33	73 ^{+9.58} _{-8.53}	36 ^{+7.06} ₋	37 ^{+7.14} _{-6.06}
005259.04-722845.5	1.925e+33	1.526e+33	5.133e+31	26 ^{+6.17} _{-5.07}	24 ^{+5.97} _{-4.87}	2 ^{+2.65} _{-1.29}
005301.38-722301.3	1.140e+33	5.770e+32	4.738e+32	7 ^{+3.78} _{-2.58}	4 ^{+3.17} _{-1.91}	3 ^{+2.93} _{-1.63}
005307.75-722359.4	1.525e+33	4.153e+31	1.624e+33	26 ^{+6.17} _{-5.07}	2 ^{+2.65} _{-1.29}	24 ^{+5.97} _{-4.87}
005310.46-722232.5	1.851e+33	7.762e+32	9.871e+32	39 ^{+7.3} _{-6.22}	22 ^{+5.76} _{-4.33}	17 ^{+5.21} _{-4.08}
005315.56-722150.4	1.119e+33	8.563e+31	1.118e+33	20 ^{+5.55} _{-4.44}	4 ^{+3.17} _{-1.91}	16 ^{+5.09} _{-3.96}
005320.49-722349.3	3.634e+33	2.783e+33	2.293e+32	59 ^{+8.72} _{-7.66}	54 ^{+8.39} _{-7.33}	5 ^{+3.39} _{-2.16}
005323.55-722354.3	6.634e+32	2.509e+32	3.907e+32	14 ^{+4.84} _{-3.7}	7 ^{+3.78} _{-2.57}	7 ^{+3.78} _{-2.58}
005327.47-722903.3	1.091e+33	5.571e+32	4.471e+32	18 ^{+5.33} _{-4.2}	13 ^{+4.7} _{-3.56}	5 ^{+3.39} _{-2.16}

luminosities and counts:

Table 4.3. Luminosities and Counts of the DF1 XRSs

Src. ID	L_x (0.5-7.0) keV	L_x (0.5-2.0) keV	L_x (2.0-7.0) keV	cnts (0.5-7.0) keV	cnts (0.5-2.0) keV	cnts (2.0-7.0) keV
005329.41-722318.8	1.535e+33	3.040e+32	1.279e+33	25 ^{+6.07} _{-4.97}	11 ^{+4.42} _{-3.27}	14 ^{+4.84} _{-3.70}
005329.95-722529.3	1.914e+33	7.498e+32	1.092e+33	27 ^{+6.26} _{-5.17}	15 ^{+4.96} _{-3.83}	12 ^{+4.57} _{-3.47}
005331.73-722240.9	2.180e+34	1.046e+34	9.837e+33	360 ^{+19.99} _{-18.97}	226 ^{+16.05} _{-15.03}	135 ^{+12.65} _{-11.61}
005332.44-722911.6	1.495e+33	2.644e+32	1.289e+33	23 ^{+5.87} _{-4.76}	7 ^{+3.78} _{-2.58}	16 ^{+5.09} _{-3.96}
005334.39-722236.8	1.467e+33	8.995e+32	3.977e+32	26 ^{+6.17} _{-5.07}	20 ^{+5.55} _{-4.44}	6 ^{+3.59} _{-2.38}
005335.77-721953.4	7.450e+32	2.342e+32	5.033e+32	23 ^{+5.87} _{-4.76}	12 ^{+4.57} _{-3.41}	11 ^{+4.4} _{-3.27}
005337.71-723144.7	1.573e+33	3.285e+32	1.288e+33	34 ^{+6.89} _{-5.8}	11 ^{+4.42} _{-3.27}	24 ^{+5.97} _{-4.87}
005337.89-722409.0	1.398e+34	6.509e+33	6.578e+33	148 ^{+13.19} _{-12.16}	92 ^{+10.63} _{-9.57}	58 ^{+8.66} _{-7.6}
005339.21-722732.3	1.295e+33	8.098e+32	3.287e+32	23 ^{+5.87} _{-4.76}	17 ^{+8.21} _{-4.08}	6 ^{+3.59} _{-2.38}
005344.45-721915.5	2.651e+33	1.161e+33	1.347e+33	20 ^{+5.55} _{-4.44}	9 ^{+4.12} _{-2.94}	11 ^{+4.42} _{-3.27}
005345.89-721947.6	1.257e+33	1.481e+32	1.184e+33	40 ^{+7.38} _{-6.3}	16 ^{+5.09} _{-3.96}	24 ^{+5.97} _{-4.87}
005348.01-723242.3	1.852e+33	8.407e+32	9.016e+32	28 ^{+6.36} _{-5.26}	16 ^{+5.09} _{-3.96}	12 ^{+4.57} _{-3.42}
005349.04-722506.3	7.687e+32	5.965e+32	3.819e+31	13 ^{+4.7} _{-8.26}	12 ^{+4.57} _{-3.42}	1 ^{+2.32} _{-0.83}
005349.69-723100.0	2.773e+33	1.096e+33	1.568e+33	47 ^{+7.91} _{-6.83}	27 ^{+6.26} _{-5.17}	20 ^{+5.55} _{-4.44}
005351.34-721818.6	1.164e+34	6.371e+33	4.189e+33	187 ^{+14.7} _{-13.67}	121 ^{+12.03} _{-10.99}	66 ^{+9.17} _{-8.11}
005352.51-723159.4	1.056e+34	3.049e+33	7.511e+33	174 ^{+14.21} _{-13.18}	77 ^{+9.81} _{-8.76}	99 ^{+10.98} _{-9.94}
005353.46-723109.0	2.382e+33	6.545e+32	1.738e+33	35 ^{+6.97} _{-5.89}	15 ^{+4.96} _{-3.83}	21 ^{+5.66} _{-4.55}
005354.88-722722.2	6.877e+32	1.499e+32	5.545e+32	14 ^{+4.84} _{-3.7}	5 ^{+3.39} _{-2.16}	9 ^{+4.12} _{-2.94}
005355.38-722645.7	3.804e+33	2.248e+33	1.143e+33	62 ^{+8.92} _{-7.86}	45 ^{+7.76} _{-6.69}	17 ^{+5.21} _{-4.08}
005357.21-722443.0	4.629e+33	2.294e+33	1.988e+33	67 ^{+9.23} _{-8.17}	43 ^{+7.61} _{-6.53}	25 ^{+6.07} _{-4.97}
005358.56-722614.7	2.023e+33	5.957e+32	1.422e+33	30 ^{+6.54} _{-5.44}	12 ^{+4.57} _{-3.42}	18 ^{+5.33} _{-4.2}
005401.03-722411.0	1.304e+33	9.168e+32	1.94e+32	21 ^{+5.66} _{-4.55}	17 ^{+5.21} _{-4.08}	4 ^{+3.17} _{-1.91}

Table 4.4. Luminosities and Counts of the DF1 XRSs

Src. ID	L_x (0.5-7.0) keV	L_x (0.5-2.0) keV	L_x (2.0-7.0) keV	cnts (0.5-7.0) keV	cnts (0.5-2.0) keV	cnts (2.0-7.0) keV
005402.00-723020.3	5.346e+32	2.909e+32	1.945e+32	11 ^{+4.42} _{-3.27}	7 ^{+3.78} _{-6.38}	4 ^{+3.17} _{-1.91}
005403.97-722632.9	3.775e+33	8.811e+32	2.965e+33	34 ^{+6.89} _{-5.8}	10 ^{+4.27} _{-3.11}	24 ^{+5.97} _{-4.87}
005405.85-722516.7	2.829e+32	2.680e+31	2.7541e+32	5 ^{+3.35} _{-2.16}	1 ^{+2.32} _{-0.83}	4 ^{+3.17} _{-1.91}
005406.07-722650.1	3.119e+33	8.784e+32	2.245e+33	21 ^{+5.66} _{-4.55}	11 ^{+4.42} _{-3.27}	10 ^{+4.27} _{-3.11}
005408.64-722356.4	4.771e+33	1.458e+33	3.279e+33	72 ^{+9.52} _{-8.47}	31 ^{+6.63} _{-5.54}	42 ^{+7.53} _{-6.46}
005409.86-722438.5	1.413e+33	1.625e+32	1.337e+33	25 ^{+6.07} _{-4.97}	4 ^{+3.17} _{-1.91}	21 ^{+5.66} _{-4.55}
005411.48-723512.3	1.182e+34	6.868e+33	3.711e+33	180 ^{+14.44} _{-13.41}	108 ^{+11.42} _{-10.38}	72 ^{+9.52} _{-8.47}
005413.61-722509.0	1.011e+33	7.299e+32	1.243e+32	4 ^{+3.17} _{-1.91}	1 ^{+2.32} _{-0.83}	3 ^{+2.93} _{-1.63}
005423.25-722345.8	5.612e+32	2.289e+32	3.079e+32	15 ^{+4.96} _{-3.83}	7 ^{+3.78} _{-2.58}	8 ^{+3.95} _{-2.77}
005425.01-722453.6	8.528e+32	6.694e+32	3.183e+31	7 ^{+3.78} _{-2.58}	5 ^{+3.39} _{-4.16}	2 ^{+2.65} _{-1.29}
005428.93-723107.1	2.533e+34	1.821e+34	3.213e+33	278 ^{+17.69} _{-16.67}	237 ^{+24.59} _{-15.39}	43 ^{+7.61} _{-6.52}
005429.01-723041.7	4.342e+33	2.082e+33	1.959e+33	63 ^{+8.98} _{-7.92}	45 ^{+7.76} _{-6.69}	18 ^{+5.33} _{-4.2}
005430.68-723008.3	4.585e+33	3.331e+33	5.358e+32	64 ^{+9.04} _{-7.98}	51 ^{+8.19} _{-7.12}	13 ^{+4.7} _{-3.56}
005437.17-722637.8	2.937e+34	1.592e+34	1.0766e+34	435 ^{+21.87} _{-20.85}	295 ^{+18.19} _{-17.17}	144 ^{+13.03} _{-11.99}
005438.53-722209.9	2.043e+33	1.036e+33	8.467e+32	42 ^{+7.53} _{-6.46}	26 ^{+6.17} _{-5.07}	16 ^{+5.09} _{-3.96}
005441.94-722952.	1.089e+33	1.620e+32	9.806e+32	23 ^{+5.87} _{-4.76}	8 ^{+3.95} _{-2.77}	15 ^{+4.96} _{-3.83}
005442.40-723058.6	1.917e+33	3.296e+32	1.666e+33	47 ^{+7.91} _{-6.83}	20 ^{+5.55} _{-4.44}	27 ^{+6.26} _{-5.17}
005445.40-722358.2	1.673e+34	7.451e+33	8.335e+33	204 ^{+15.3} _{-14.27}	125 ^{+12.21} _{-11.17}	79 ^{+9.93} _{-8.87}
005446.33-722523.3	8.473e+33	2.911e+33	5.3898e+33	145 ^{+13.07} _{-12.03}	66 ^{+9.17} _{-8.11}	80 ^{+9.96} _{-8.93}
005447.11-722722.2	2.661e+33	1.052e+33	1.506e+33	42 ^{+7.52} _{-6.46}	26 ^{+6.17} _{-5.07}	16 ^{+5.09} _{-3.96}
005448.95-722544.8	8.952e+33	5.336e+3	2.628e+33	138 ^{+12.77} _{-11.74}	98 ^{+10.93} _{-9.88}	41 ^{+7.46} _{-6.38}
005451.24-722631.3	2.598e+34	9.822e+33	1.531e+34	399 ^{+20.99} _{-19.96}	191 ^{+14.84} _{-13.80}	208 ^{+15.44} _{-14.41}
005504.40-722230.3	8.983e+3	4.734e+33	3.477e+33	149 ^{+13.23} _{-12.2}	88 ^{+10.42} _{-9.58}	62 ^{+8.92} _{-7.86}
005507.84-722241.8	9.132e+33	3.116e+33	5.837e+33	128 ^{+12.34} _{-11.3}	53 ^{+8.33} _{-7.26}	77 ^{+9.81} _{-8.76}
005532.53-722442.1	4.301e+3	1.059e+33	3.302e+33	76 ^{+9.76} _{-8.7}	46 ^{+7.83} _{-6.76}	30 ^{+6.54} _{-5.46}

Table 4.5. Luminosities and Counts of the DF2 XRSs

Src. ID	L_x (0.5-7.0) keV	L_x (0.5-2.0) keV	L_x (2.0-7.0) keV	cnts (0.5-7.0) keV	cnts (0.5-2.0) keV	cnts (2.0-7.0) keV
004920.98-731740.8	9.778e+33	4.934e+33	5.564e+33	70 ^{+9.41} _{-17.35}	35 ^{+6.97} _{-5.85}	36 ^{+7.06} _{-5.97}
004929.75-731150.4	6.120e+33	2.332e+33	3.970e+33	51 ^{+8.19} _{-7.12}	19 ^{+5.44} _{-4.32}	32 ^{+6.72} _{-5.63}
004941.98-732314.6	4.923e+35	1.902e+35	3.177e+35	3860 ^{+63.13} _{-62.13}	1363 ^{+37.92} _{-36.92}	2507 ^{+51.07} _{-50.07}
004948.21-732211.4	4.711e+34	2.935e+34	2.320e+34	429 ^{+21.73} _{-20.71}	231 ^{+16.22} _{-15.18}	200 ^{+15.16} _{-14.13}
004950.30-731306.7	4.215e+33	2.560e+33	2.118e+33	16 ^{+5.09} _{-3.96}	2 ^{+2.65} _{-1.29}	14 ^{+4.84} _{-3.7}
004952.26-731743.3	2.016e+33	8.918e+32	1.228e+33	17 ^{+5.21} _{-4.08}	9 ^{+4.12} _{-2.94}	8 ^{+3.95} _{-2.77}
004957.24-731655.2	5.509e+33	3.744e+33	2.512e+33	50 ^{+8.12} _{-7.05}	25 ^{+6.07} _{-4.97}	25 ^{+6.07} _{-4.97}
005004.11-731814.0	1.564e+33	9.379e+32	7.940e+32	16 ^{+5.09} _{-3.96}	8 ^{+3.95} _{-2.77}	8 ^{+3.95} _{-2.77}
005005.25-731145.7	6.452e+33	3.772e+33	3.338e+33	68 ^{+9.29} _{-8.23}	33 ^{+6.8} _{-5.72}	35 ^{+6.97} _{-5.89}
005006.54-731549.6	3.943e+33	2.883e+33	1.667e+33	40 ^{+7.38} _{-6.3}	24 ^{+5.97} _{-4.87}	16 ^{+5.09} _{-3.96}
005010.02-731931.3	3.713e+33	3.165e+33	1.279e+33	26 ^{+6.17} _{-5.07}	17 ^{+5.21} _{-4.08}	9 ^{+4.12} _{-2.94}
005014.09-731351.2	1.306e+33	1.449e+32	1.075e+33	8 ^{+3.95} _{-2.77}	2 ^{+2.65} _{-1.29}	6 ^{+3.59} _{-2.38}
005016.36-732233.7	2.670e+33	8.047e+32	1.870e+33	25 ^{+6.07} _{-4.97}	12 ^{+4.57} _{-3.42}	13 ^{+4.07} _{-3.56}
005020.44-731116.6	3.112e+33	4.723e+32	2.480e+34	45 ^{+7.76} _{-6.69}	1 ^{+2.32} _{0.83}	44 ^{+7.68} _{-6.61}
005028.17-732622.9	9.278e+33	1.437e+33	7.374e+33	95 ^{+10.78} _{-9.73}	42 ^{+7.53} _{-6.46}	55 ^{+8.46} _{-7.4}
005036.10-731739.3	6.559e+34	7.045e+33	5.490e+33	101 ^{+11.08} _{-10.04}	51 ^{+8.19} _{-7.12}	50 ^{+8.12} _{-7.05}
005044.67-731605.1	2.333e+35	9.692e+34	1.462e+35	2030 ^{+46.06} _{-45.06}	773 ^{+28.81} _{-27.8}	1264 ^{+36.56} _{-35.55}
005045.03-731539.6	1.363e+34	1.058e+34	5.366e+33	134 ^{+12.6} _{-11.56}	83 ^{+10.15} _{-9.1}	51 ^{+8.19} _{-7.12}
005047.95-731817.8	7.629e+33	6.018e+33	2.942e+33	34 ^{+6.89} _{-5.8}	12 ^{+4.57} _{-3.42}	22 ^{+5.76} _{-4.66}
005054.33-731741.9	1.281e+33	1.950e+32	1.021e+33	12 ^{+4.57} _{-3.42}	2 ^{+2.65} _{-1.29}	10 ^{+4.27} _{-3.11}
005059.09-732055.3	9.348e+33	1.280e+33	7.538e+33	93 ^{+10.68} _{-9.63}	25 ^{+11.07} _{-4.97}	68 ^{+9.29} _{-8.23}

Table 4.6. Luminosities and Counts of the DF2 XRSs

Src. ID	L_x (0.5-7.0) keV	L_x (0.5-2.0) keV	L_x (2.0-7.0) keV	cnts (0.5-7.0) keV	cnts (0.5-2.0) keV	cnts (2.0-7.0) keV
005102.37-731608.7	1.941e+33	3.687e+32	1.498e+33	11 ^{+4.42} _{-3.27}	3 ^{+2.93} _{-1.63}	8 ^{+3.95} _{-2.77}
005110.29-731335.4	8.970e+33	4.873e+33	4.881e+33	66 ^{+9.17} _{-8.11}	30 ^{+6.45} _{-5.45}	37 ^{+7.14} _{-6.06}
005117.06-731606.8	7.701e+32	8.134e+32	1.640e+32	9 ^{+4.12} _{-2.94}	7 ^{+3.78} _{-2.58}	2 ^{+2.65} _{-1.29}
005132.63-731411.4	5.927e+33	2.272e+33	3.836e+33	25 ^{+6.07} _{-4.97}	11 ^{+4.42} _{-3.27}	14 ^{+4.84} _{-3.7}
005139.76-731802.4	6.217e+33	2.358e+33	4.040e+33	53 ^{+8.33} _{-7.56}	20 ^{+5.55} _{-4.44}	33 ^{+6.8} _{-5.72}
005144.89-731439.9	1.690e+33	9.736e+32	8.840e+32	23 ^{+5.87} _{-4.76}	11 ^{+4.42} _{-3.27}	12 ^{+4.57} _{-3.42}
005151.11-731751.8	1.375e+33	1.129e+33	5.014e+32	22 ^{+5.76} _{-4.66}	14 ^{+4.84} _{-3.7}	8 ^{+3.95} _{-2.77}
005152.01-731033.6	5.029e+35	3.337e+35	2.345e+35	3054 ^{+56.26} _{-55.26}	1521 ^{+40.00} _{-39.00}	1539 ^{+40.23} _{-39.23}
005201.93-731405.5	8.742e+33	3.606e+33	5.494e+33	89 ^{+10.47} _{-9.53}	39 ^{+7.3} _{-6.22}	51 ^{+8.19} _{-7.12}
005214.03-731918.7	1.294e+34	6.005e+33	7.707e+33	144 ^{+13.03} _{-11.99}	58 ^{+8.66} _{-7.6}	86 ^{+10.31} _{-9.26}
005219.10-731939.6	6.404e+33	1.852e+33	4.535e+33	56 ^{+8.53} _{-7.46}	16 ^{+5.06} _{-3.96}	40 ^{+7.38} _{-6.3}
005316.63-731639.2	1.675e+34	2.243e+34	5.100e+32	46 ^{+7.83} _{-6.76}	18 ^{+5.33} _{-4.2}	28 ^{+6.36} _{-5.26}

Chapter 5

Results:

5.1 X-ray Color Magnitude Diagrams:

We first attempt to identify candidate quiescent NS LMXBs through producing X-ray color-magnitude diagrams. (Optical) color-magnitude diagrams (CMDs) plot stellar color (e.g. $B-V$, to find how blue a star is) vs. brightness (in magnitudes), and are a standard tool of optical astrophysics. X-ray CMDs [24] are designed similarly, plotting (inferred) X-ray luminosity vs. an X-ray color, where the color is generally designed to be either the ratio of counts in two energy bands, or the logarithm of this ratio. These diagrams separate sources by L_X and X-ray color, which has proved useful in identifying quiescent NS LMXBs in GCs [46]. One must be careful to recognize that the inferred L_X may be incorrect if the X-ray source is not at the distance considered (e.g. a foreground Galactic star), and that the X-ray color and luminosity are influenced by gas and dust (which “hardens” the spectrum by removing soft photons) between the X-ray source and the Earth.

To produce X-ray CMDs, we plot the inferred 0.5-7 keV L_X vs. an X-ray “hard-

ness” color, defined as $2.5 \log([0.5-2.0 \text{ keV}]/[2.0-7.0 \text{ keV}])$ (higher values are softer), for both DF1 and DF2, using the plotting package Super Mongo¹. We also calculated the predicted positions of quiescent NS LMXBs with hydrogen atmospheres (modified blackbody spectra, see section 3.5), as calculated with the NSATMOS spectrum [82]. NSs in the SMC should be located on a well-defined cooling track, defined by the NSs’ distance, radius, and mass, with the temperature uniquely determining both an X-ray color and L_X . However, if the quiescent NS LMXBs show a substantial contribution from the harder spectral component (in addition to radiation from the NS surface), their colors will shift to harder values. We plot the expected locations of NSs with hydrogen atmospheres in our X-ray CMDs from DF1 and DF2, in Figs. 5.1 and 5.2.

From the diagrams we see that few X-ray sources coincide exactly with the track for NS atmospheres. However, we also can see that a good number of sources are consistent with the track within their 1σ errors, and more within 2σ . We identify 10 sources which have relatively soft spectra (within 2σ of the NS atmosphere tracks) and L_X in the range of $6 \times 10^{32} \text{ ergs}^{-1} < L_x < 10^{34} \text{ ergs}^{-1}$, which are possible candidates for quiescent NS LMXBs. In Table 4.1, we include the photometry for these candidate sources.

¹<http://www.astro.princeton.edu/~rhl/sm/sm.html>

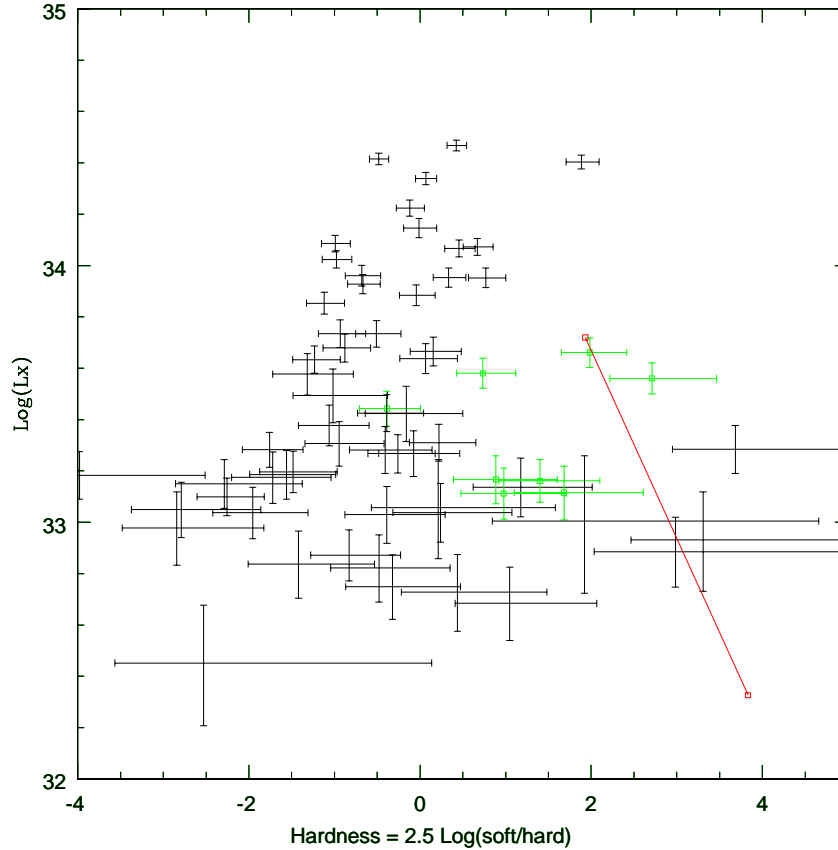


Figure 5.1 XCMD of DF1

It's plotting the inferred 0.5-7 keV X-ray luminosity L_X vs. an X-ray “hardness” color, defined as $2.5 \log([0.5 - 2.0 \text{ keV}]/[2.0 - 7.0 \text{ keV}])$ (higher values are softer). The red track is the predicted positions of quiescent NS LMXBs with hydrogen atmospheres (modified blackbody spectra), as calculated with the NSATMOS spectrum. The candidates for quiescent NS LMXBs are labeled with tiny box on their positions with green colour. There are 8 candidates on this field which have reasonable counts and more softness than others and also not very far from the red track.

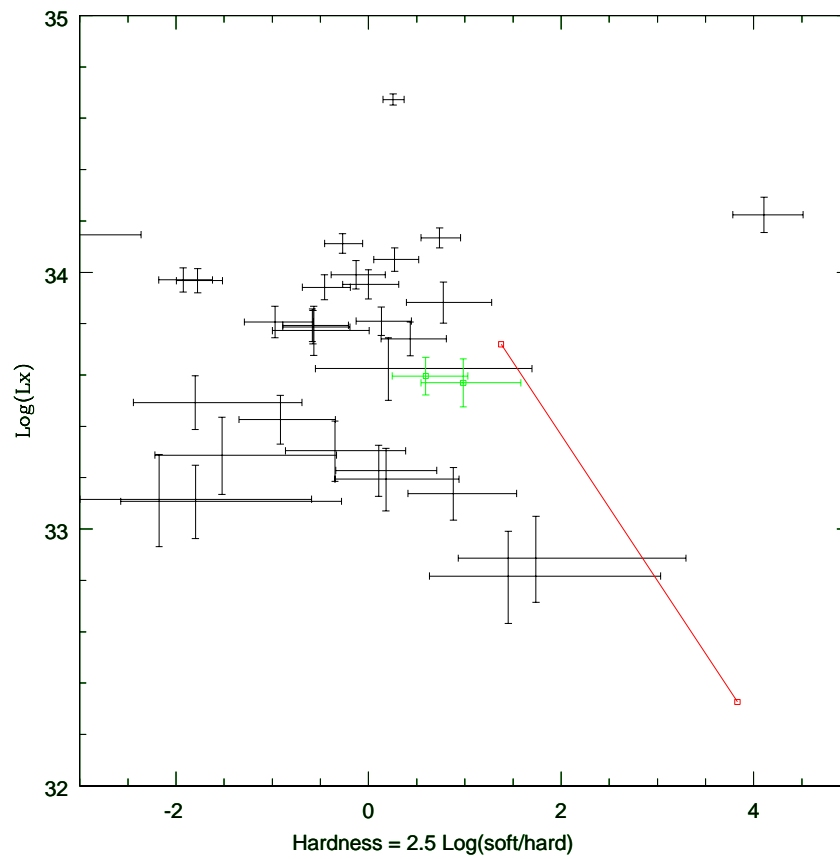


Figure 5.2 XCMD for DF2

It is plotted as Fig. 5.1 . There are 2 potential candidates for the quiescent NS LMXBs in this field marked as tiny box on their position and green color.

5.2 Spectral Fitting Of Candidates:

To refine our selection of candidates, we fit the spectra of our candidate quiescent LMXBs with several spectral models. We fit spectra between 0.5 and 7 keV (chosen to avoid calibration uncertainties below 0.5 keV, and relatively low signal-to-noise ratios above 7 keV), using the XSPEC fitting package ².

For sources with > 40 counts, we bin the data by at least 5 counts/bin, permitting the use of the χ^2 statistic. Sources with < 40 counts were analyzed without binning the data, forcing the use of the C statistic³, a maximum-likelihood estimator [81]. The C statistic allows parameter estimation and the identification of confidence levels, but does not provide a goodness-of-fit criterion. We fill this gap by using Monte Carlo simulations of the best-fit spectrum, to determine if the observed C statistic is unusually high with respect to the statistic value for simulated spectra—this would indicate a poor fit.

We choose three models to analyze the spectra of these sources: a simple power law ($F_\nu \propto \nu^{\Gamma-1}$ with Γ , the photon index, variable), a thermal plasma MEKAL spectrum [84] and a two-component model of a hydrogen-atmosphere NS model [82] joint with a power-law, which is physically appropriate for quiescent NS LMXB spectra. To simplify our analysis in the case of nsatmos+power-law fitting, we fixed the photon index associated to the power-law model as 1.5 [46], the NS radius to 10 km (the canonical value; the true value is unknown), the mass to $1.4 M_\odot$, and the distance to 63 kpc. We also fixed the N_H column associated with this model to $N_H = 0.15 \times 10^{22} \text{ cm}^{-2}$, a typical value for the SMC. For sources with steep power-law fits (photon index $\Gamma \geq 2.45$), we have performed MEKAL fitting which can be physically appropriate

²<http://heasarc.gsfc.nasa.gov/docs/xanadu/xspec/index.html>

³<http://heasarc.gsfc.nasa.gov/docs/xanadu/xspec/manual/XSappendixCash.html>

for CVs or ABs [92].

The results of the spectral fitting are summarized in the tables 5.2, & 5.3. Table 5.2 shows the power-law fitting, and also gives the two-component model of power-law+nsatmos, and Table 5.3 gives the results of MEKAL model fitting. The 2nd column of the tables gives the value of the absorbing column density N_H which is left free for all models except in Table 5.2 for power-law+nsatmos fits. The 3rd column in Table 5.2 is the photon index Γ which is fixed for the two-component model to 1.5, the effective temperature of the NS surface, kT, is given in the 4th column, and the last column is the 'Goodness', the fraction of simulations with fit statistic smaller than the data's (a very high number indicates a poor fit).

Considering the power-law fits (Table 5.2, we see that three sources (005232.28-722607.7, 005339.39-722732.3, and 005010.02-731931.3) are poorly fit by power-law models, while another two sources (005320.49-722349.3 and 005334.39-722236.8) require $\Gamma \gg 2$. As most classes of X-ray source can be fit by relatively hard power-law models (including background active galactic nuclei, high-mass X-ray binaries, CVs, luminous chromospherically active binaries, radio pulsars, etc. etc.), ruling out such a fit leaves few remaining classes of objects. The most likely candidates are probably low- L_X (thus probably Galactic) chromospherically active stars, and quiescent NS LMXBs. Alternative possibilities include strongly magnetic (so-called "polar") CVs, which can reach $L_x > 10^{32}$ ergs/s with soft blackbody-like spectra from accretion onto their magnetic poles (e.g. RX J1007-20, Ramsay & Cropper 2003 [98];

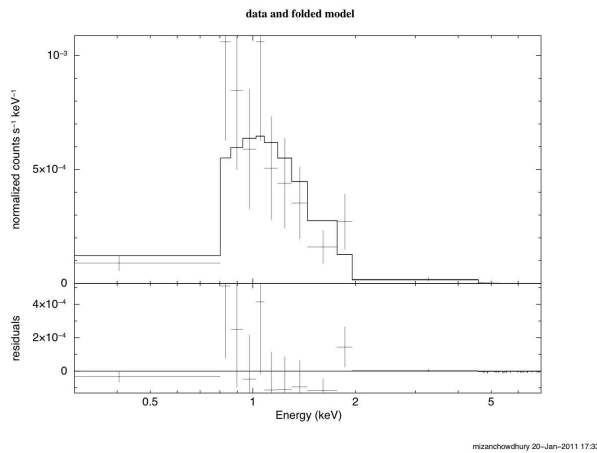
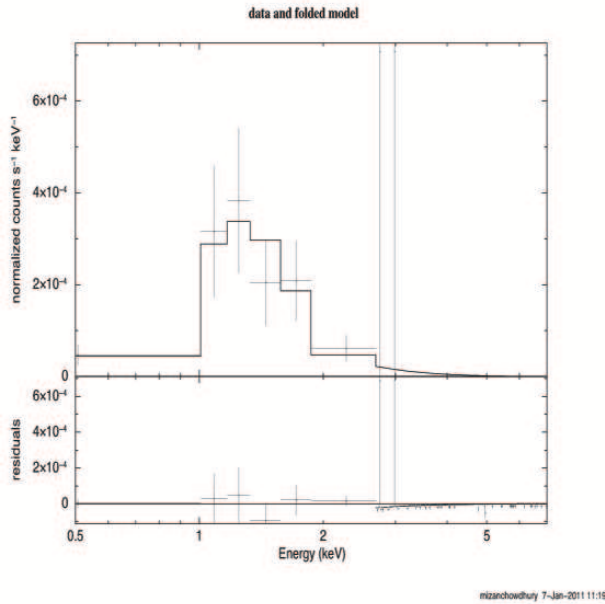


Figure 5.3 Power-law fit
 X-ray spectrum of 2 candidates fitted with an absorbed power-law model. The top is the observation of CXOU J005232.28-722607.7 and the bottom is the CXOU J005320.49-722349.3. In each figure there are two parts the top gives the absorbed power-law and the bottom gives the residuals to fits.

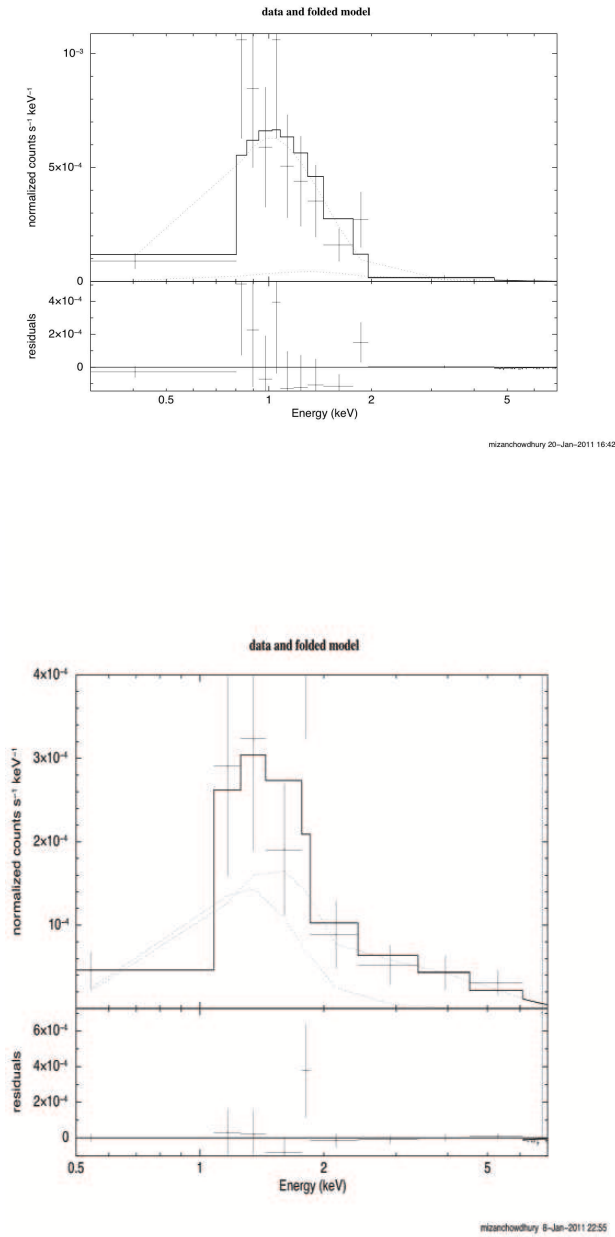


Figure 5.4 Power-law+nsatmos fit
 X-ray spectrum of 2 candidates, showing data(crosses),model(solid line), and fitted with an absorbed hydrogen atmosphere NS model and a power-law as in Table 5.2 with an fixed photon index 1.5. The candidates are on top : CXOU J005320.49-722349.3 and on the bottom .

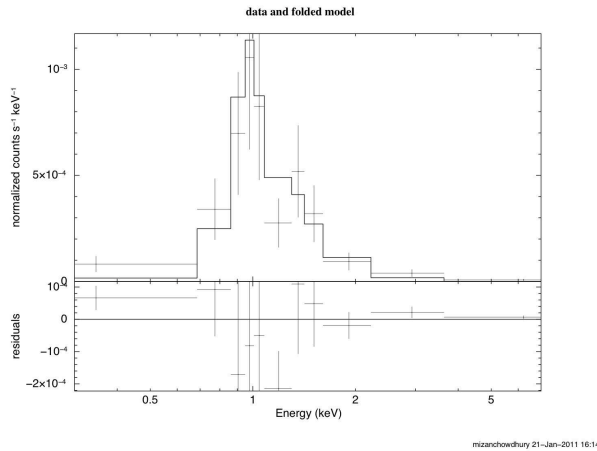
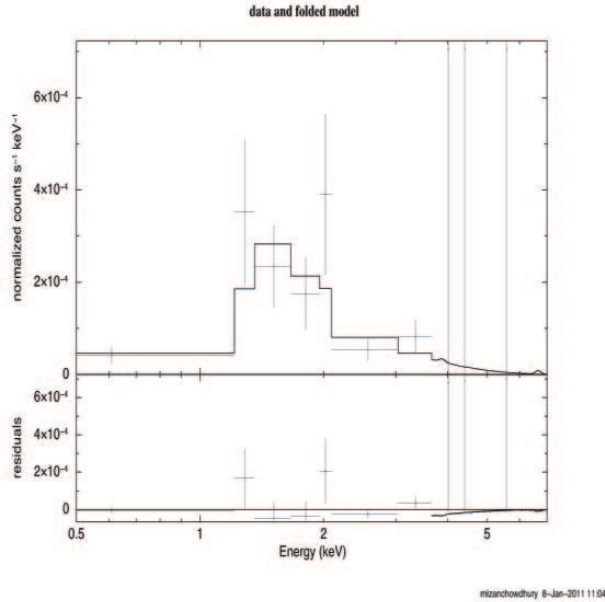


Figure 5.5 MEKAL fit

Energy spectra of the 2 candidates fitted with a thermal plasma MEKAL model. The observations are top t: CXOU J 005006.54-731549.6 , and bottom: CXOU J005430.68-723008.3.

X10 in 47 Tuc, [92]. We turn next to the power-law+NSATMOS fits, to see whether these sources can be well-fit by models appropriate for quiescent NS LMXBs. We note that source 005010.02-731931.3, when fit by this model, produces a best-fit NS atmosphere component temperature equal to the lower boundary of the search space ($\log T_{eff}=5.0$, essentially zero), along with two of the sources which were well-fit by simple absorbed power-law models. This does not prove that 005010.02-731931.3 is not a quiescent NS LMXB, but it indicates that there is no evidence for a NS atmosphere component in its spectrum. Thus we remain with four candidate quiescent NS LMXBs.

Finally, we consider the MEKAL spectral fits. These fits may be appropriate for nearby chromospherically active binaries, and will be distinguished from simple power-laws by the presence of line emission, typically from Fe L-shell electrons near energies of 1 keV for plasma temperatures below a few keV. Here we find that sources 005232.28-722607.7 and 005320.49-722349.3 cannot be well-fit by single-temperature spectral fits, while 005334.39-722236.8 is well-fit by these models. Thus the first two must be considered better candidates for quiescent NS LMXBs than the latter, as a reasonable MEKAL fit may be evidence for a nature as a normal star.

These spectral fits do not conclusively prove that these sources are or are not quiescent NS LMXBs, but they suggest that some sources are reasonable candidates, and others are less likely.

Table 5.1. Luminosities and Counts of the candidates

Src. ID	L_x (0.5-7.0) keV	L_x (0.5-2.0) keV	L_x (2.0-7.0) keV	cnts (0.5-7.0) keV	cnts (0.5-2.0) keV	cnts (2.0-7.0) keV
005232.28-722607.7	1.45e+33	9.80e+32	2.69e+32	32 ^{+6.72} _{-5.62}	26 ^{+6.17} _{-5.06}	6 ^{+3.59} _{-2.37}
005320.49-722349.3	3.63e+33	2.78e+33	2.29e+32	59 ^{+8.72} _{-7.65}	54 ^{+8.39} _{-7.32}	5 ^{+3.39} _{-2.15}
005349.69-723100.0	2.77e+33	1.09e+33	1.56e+33	47 ^{+7.91} _{-6.82}	27 ^{+6.26} _{-5.16}	20 ^{+5.55} _{-4.43}
005339.21-722732.3	1.29e+33	8.09e+32	3.28e+32	23 ^{+5.87} _{-4.75}	17 ^{+5.21} _{-4.07}	6 ^{+3.59} _{-2.374}
005334.39-722236.8	1.46e+33	8.99e+32	3.97e+32	26 ^{+6.17} _{-5.06}	20 ^{+5.55} _{-4.43}	6 ^{+3.59} _{-2.37}
005355.38-722645.7	7.32e+33	7.38e+33	1.78e+33	62 ^{+8.92} _{-7.85}	45 ^{+7.76} _{6.68}	17 ^{+5.21} _{-4.07}
005401.03-722411.0	1.30e+33	9.16e+32	1.94e+32	21 ^{+5.66} _{-4.54}	17 ^{+5.21} _{-4.07}	4 ^{+3.17} _{-1.90}
005430.68-72300.83	4.58e+33	3.33e+33	5.36e+32	64 ^{+9.04} _{-7.98}	51 ^{+8.19} _{-7.12}	13 ^{+4.7} _{-3.56}
005010.02-731931.3	3.71e+33	3.16e+33	1.27e+33	26 ^{+6.17} _{-5.06}	17 ^{+5.21} _{-4.07}	9 ^{+4.12} _{-2.93}
005006.54-731549.6	3.94e+33	2.88e+33	1.66e+33	40 ^{+7.38} _{-6.29}	24 ^{+5.97} _{-4.86}	16 ^{+5.092} _{-3.95}

Table 5.2. Spectral model parameters

Src ID	$N_H \times 10^{22}$	Γ	kT(keV)	goodness
Power law				
005232.28-722607.7	$1.34^{+0.76}_{-0.81}$	$5.00^{+1.71}_{-1.98}$...	100%
005320.49-722349.3	$0.50^{+0.29}_{-0.37}$	$4.9^{+1.40}_{-1.70}$...	11%
005349.69-723100.0	$0.44^{+0.89}_{-0.43}$	$1.9^{+1.02}_{-0.86}$...	55.23%
005339.39-722732.3	$0.30^{+0.62}_{-0.30}$	$2.31^{+1.51}_{-1.20}$...	100%
005334.39-722236.8	$0.74^{+0.89}_{-0.61}$	$4.2^{+2.9}_{-1.9}$...	20.14%
005355.38-722645.7	$0.25^{+0.62}_{-0.23}$	$2.5^{+0.83}_{-0.73}$...	58.17%
005401.03-722411.0	$0.17^{+0.57}_{-0.17}$	$2.44^{+2.69}_{-1.10}$...	15.43%
005430.68-72300.83	$0.16^{+0.51}_{-0.02}$	$2.806^{+2.07}_{-0.68}$...	2.84%
005010.02-731931.3	$0.57^{+0.72}_{-0.50}$	$2.43^{+1.35}_{-1.13}$...	100%
005006.54-731549.6	$1.16^{+1.05}_{-0.73}$	$3.03^{+1.41}_{-1.17}$...	20.42%
Power law+NSATMOS				
005232.28-722607.7	$6.14^{+0.05}_{-0.21}$	88.81%
005320.49-722349.3	$6.23^{+0.02}_{-0.03}$	21.34%
005349.69-723100.0	$5.00^{+1.09}_{-5.00}$	44.02%
005339.39-722732.3	$6.02^{+0.10}_{-6.02}$	8.04%
005334.39-722236.8	$6.15^{+0.04}_{-0.07}$	84.79%
005355.38-722645.7	$6.17^{+0.04}_{-0.07}$	9.80%
005401.03-722411.0	$6.09^{+0.05}_{-0.14}$	99.26%
005430.68-72300.83	$5.96^{+0.26}_{-0.31}$	13.75%
005010.02-731931.3	$5.03^{+1.04}_{-5.01}$	14.4%
005006.54-731549.6	$5.00^{+1.04}_{-5.00}$	82.15%

Table 5.3. Spectral model parameters
-continued-

Src ID	$N_H \times 10^{22}$	Γ	kT(keV)	goodness
MEKAL				
005232.28-722607.7	$1.63^{+0.53}_{-0.73}$...	$0.54^{+0.60}_{-0.17}$	99.90%
005320.49-722349.3	$0.66^{+0.20}_{-0.25}$...	$0.55^{+0.14}_{-0.14}$	100%
005349.69-723100.0	$0.16^{+0.76}_{-1.66}$...	$7.69^{+4.93}_{-7.56}$	15.84%
005334.39-722236.8	$1.06^{+0.69}_{-0.34}$...	$0.66^{+0.47}_{-0.29}$	35.38%
005339.39-722732.3	$0.15^{+0.39}_{-0.15}$...	$3.08^{+3.08}_{-1.28}$	89.77%
005355.38-722645.7	$0.04^{+0.18}_{-0.04}$...	$3.28^{+4.50}_{-1.24}$	16.84%
005401.03-722411.0	$0.008^{+0.28}_{-0.007}$...	$3.05^{+11.25}_{-1.51}$	100.00%
005430.68-72300.83	$0.567^{+0.38}_{-0.53}$...	$0.80^{+0.58}_{-0.33}$	18.29%
005010.02-731931.3	$0.46^{+0.96}_{-0.47}$...	$2.97^{+2.94}_{-1.85}$	12.9%
005006.54-731549.6	$1.25^{+0.98}_{-0.84}$...	$1.65^{+3.12}_{-0.73}$	71.64%

5.3 Comparison With Optical Counterpart Lists:

If soft X-ray sources are associated with nearby chromospherically active stars, they should be identifiable as relatively bright optical stars, perhaps in existing catalogues. For instance, an M5 red dwarf star ($M_V \sim 13$) at 300 pc (the thin disk scale height) will have $V \sim 20$. Some M dwarfs have $L_X \sim 2 \times 10^{28}$ ergs/s [85]; at 300 pc those would have $F_X = 1.9 \times 10^{-15}$ ergs cm $^{-2}$ s $^{-1}$, around our detection limit. Such low- L_X coronally active stars will have soft, line-dominated X-ray spectra [86]. Using the local luminosity function [87], we estimate 0.052 M stars pc $^{-3}$, which would give 10 M stars within each of our surveyed volumes out to 300 pc from Earth; a few of these will be X-ray bright enough to contaminate our sample.

We first turn to the work of Antoniou et al. (2009), who identified the optical counterparts of Chandra sources using the shallow Chandra survey of the SMC bar, which includes the sky surveyed by, and some of the X-ray sources in, the Chandra SMC deep fields. Antoniou et al. cross-correlated the coordinates of Chandra sources with the OGLE-II [88]⁴ and Magellanic Clouds Photometric Survey (MCPS, [89]) optical catalogs, which each contain photometry for millions of stars in the SMC. The MCPS survey is essentially complete to $V \sim 20$ and covers the surveyed area, and thus can serve as an effective screen for nearby Galactic stars. The OGLE-II survey reaches similar depth, but does not cover our surveyed area completely. Quiescent NS LMXBs will typically have $M_V \sim 6-8$, and thus $V \sim 25-27$ at the distance of the SMC, beyond the reach of these surveys and only barely reachable with deep HST imaging of these fields (obtained in 2006, PI A. Zezas, but not yet analyzed).

Antoniou et al. (2009) cross-correlated the Chandra coordinates with both cata-

⁴<http://ogle.astrouw.edu.pl/>

logues using average search radii of 2". They found matches to sources 4_24 and 5_16, corresponding to our sources 005010.02-731931.3 and 005355.38-722645.3, indicating that these sources are probably not quiescent LMXBs. Antoniou et al. show that 005355.38-722645.3 has optical colours corresponding to a Be XRB, while the other source is tentatively identified as an AGN in the SIMBAD Astronomical Database⁵. If the identification is correct, 005355.38-722645.3 has a relatively soft spectrum for a Be XRB in quiescence.

For our candidate quiescent LMXBs, we searched in the MCPS database to place limits on the brightness of their optical counterparts. We did not find additional counterparts in the MCPS catalogue (besides the two counterparts previously identified by Antoniou et al.).

5.4 The X-ray To Optical Flux Ratio:

The ratio of the X-ray flux to the optical flux is a useful distance-independent criterion for objects detected in the optical and X-ray wavelength bands [25]. Quiescent NS LMXBs have higher ratios of the X-ray flux to optical flux than any other known GC source class [90,91]. Here we calculated F_x in the energy range 0.5-2.5 keV and the optical flux F_{opt} values were calculated using $F_{opt} = 10^{-0.4V-5.43}$ where V is the visual magnitude. As we have considered the OGLE-II and MCPS catalogues for our optical counterpart comparison, here we use the limiting value of $V \sim 20$ to estimate the $F_{opt} = 10^{-0.4V-5.43}$ for the sources which have no identified optical counterparts. Our sources have $L_X(0.5-2.5 \text{ keV})$ between 6×10^{32} and 6×10^{33} ergs/s. Therefore we find a range of lower limits on F_X/F_{opt} from 0.35 down to 0.035 for the unidentified

⁵<http://simbad.u-strasbg.fr/simbad/>

sources, vs. values of 0.4 for 005010.02-731931.3 and 0.009 for 005355.38-722645.7.

We can compare these values with F_X/F_{Opt} values for other source classes in the literature. The few quiescent LMXBs with known optical counterparts have F_X/F_{Opt} values above 10, while CVs have $F_X/F_{Opt} \sim 1$, and chromospherically active binaries have $F_X/F_{Opt} < 1$, with the vast majority below 0.01 [90]. From this information alone, our candidates could conceivably be CVs or active binaries. However, the CVs and active binaries known with $L_X > 10^{32}$ ergs/s (the only such systems in the SMC we could detect) also generally have very hard spectra [92], and thus are generally excluded. The exception is polar CVs, which often have high F_X/F_{Opt} ratios [92, 93].

The particular goal of these F_X/F_{Opt} calculations is to exclude nearby normal M dwarf stars. We can compare with Fig. 6 of Schmitt & Liefke (2004) [85], which plots absolute magnitude vs. X-ray luminosity for nearby stars, finding there that F_X/F_{Opt} for faint M dwarfs reaches a maximum of 1. So unfortunately we can't completely rule out nearby M dwarfs with our F_X/F_{Opt} results.

Chapter 6

Constraints On The Quiescent NS LMXB Population Of The SMC:

We have identified five reasonable candidate quiescent NS LMXBs in the SMC, which have X-ray colors, X-ray spectra, and F_X/F_{Opt} values in agreement with identified quiescent NS LMXBs. Unfortunately we cannot rule out that these objects could be some other types of sources—polar CVs in the SMC and M dwarfs in our Galaxy are the most likely possibilities. Analysis of deep HST imaging of the SMC can provide much deeper limits (down to $V=25$) on optical counterparts, and thus rule out M dwarfs. Ruling out polar CVs would require longer Chandra or XMM observations to provide higher-statistics spectra.

With these caveats in mind, we proceed to estimate what our identifications, or upper limits, would entail for the total number of quiescent NS LMXBs in the SMC, and the duty cycle of NS LMXBs in old, non-GC stellar populations.

6.1 Fraction Of Quiescent NS LMXBs Detectable:

First we compute the fraction of quiescent NS LMXBs that could be detectable in our survey. We use the quiescent NS LMXB luminosity function observed in GCs from Heinke et al. (2003) [46], though with the caveat that the luminosity function in GCs may differ from that in the SMC and Galaxy. We also note that Heinke et al. (2003) [46] cannot identify quiescent LMXBs dominated by the power-law spectral component; following Heinke et al. (2005) we guess that half of all quiescent NS LMXBs are missed by searching for the soft component spectra.

Our luminosity limit is $L_X \sim 4 \times 10^{32}$ ergs/s, but for comparison of X-ray colors and spectra we realistically need at least 20 counts, which translates to 10^{33} ergs/s at the distance of the SMC. Three of 15 NS LMXBs in Heinke et al. (2003) [46] have L_X above this value; when combined with the missed NS LMXBs that have harder spectra, we estimate we may be able to detect $\sim 10\%$ of the quiescent NS LMXBs in the SMC. This estimate has a number of large uncertainties, as mentioned above, but is the best that can be done at the moment.

6.2 Computation Of Stellar Mass In SMC Deep Fields:

Next we calculate the amount of stellar mass that we have surveyed in the SMC deep fields. We use the 2MASS(Two Micron All Sky Survey, [94] infrared number counts (preferred over total IR flux in order to avoid overweighting bright stars) to estimate the fraction of the SMC's stellar mass contained within the two Deep Field regions. P.R. Wood [95] shows a CMD of the LMC (similar distance modulus as the SMC)

which we use for planning purposes. The 2MASS survey measures stars reliably down to $J \sim 16$, so we use stars with $J = 10$ to 16 for our number counts ($J \sim 10$ is the red supergiants). Wood's Fig. 2 shows that crowding does not cause significant effects in the deepest 2MASS images.

We use IPAC's Gator service ¹ to query the 2MASS database for the number of stars in different regions with $10 < J < 16$, SNR_J (signal-to-noise ratio) > 10 , and $Gal_contam < 1$. The Gal_contam contains flags for extended galaxies; neither the Gal_contam nor the SNR_J requirements had significant effects on the numbers of sources obtained. We found 1676 stars meeting our criteria within the Deep Field 1 footprint, and 2623 stars within the Deep Field 2 footprint. A few percent of these are not detected in K, from inspection of the outputs. We queried background regions several degrees away from the SMC, finding an average number of foreground/background sources of 0.6 arcmin^{-2} ; subtracting this gives 3992 stars in our studied fields. We found (background-subtracted) 54017 stars within 1 degree of the SMC's center, and 81540 stars within a box 3.017 by 2.708 degrees. Inspection of wide-field DSS (Digitized Sky Survey) images suggests this contains the vast majority of SMC stars; we guess that we may have missed 10%, so estimate 90600 giant stars ($10 < J < 16$) in the SMC. Thus our survey footprint covers about 4.4% of the SMC stellar population. Bekki & Stanimirovic (2009) [96] estimate the total luminosity $L(\text{SMC}) \sim 4.3 \times 10^8 L_{\odot}$. They also prefer a stellar-mass-to-light ratio of 2.3, appropriate if the majority of the SMC's stars are about 5 Gyrs old. This suggests $M(\text{SMC}) \sim 10^9 M_{\odot}$. Applying our ratio above gives a surveyed stellar mass of $4.4 \times 10^7 M_{\odot}$ in the two Deep Fields.

If we have detected 5 quiescent NS LMXBs, and were sensitive to 10% of these

¹<http://irsa.ipac.caltech.edu/>

LMXBs in our surveyed area, then we can estimate $50/4.4 \times 10^7 \sim 10^{-6}$ quiescent NS LMXBs per solar mass in the SMC. This suggests that there are 1000 qLMXBs in the SMC. This is a very rough estimate, and if some of these systems are not truly LMXBs (probable), then this frequency is an upper limit.

6.3 Duty Cycle Of The Quiescent NS LMXBs:

No bright LMXB has yet been detected in the SMC. So to calculate the duty cycle of NS LMXBs we must refer to the LMC and Milky Way LMXB populations. In the Milky Way there are ~ 100 bright ($L_X > 10^{36}$ ergs/s) LMXBs, and there are two in the LMC (see section 3.9). For the LMC and Milky Way the stellar mass-to-light ratio is ~ 2 [97], and the inferred stellar masses are thus $4 \times 10^9 M_\odot$ and $3 \times 10^{10} M_\odot$, respectively (using their luminosities from Sparke & Gallagher 2007 [87]). We can thus infer the number of bright LMXBs per solar mass to be 5×10^{-10} in the LMC (with large errors), and 3×10^{-9} in the Milky Way.

Comparing these values with the upper limit on the number of quiescent NS LMXBs in the SMC, we can place lower limits on the NS LMXB duty cycle, the fraction of time spent in outburst, which is (for small fractions) the number of bright LMXBs divided by the number of quiescent LMXBs. (Another caveat is that some fraction of these bright LMXBs are black hole systems, which we are not sensitive to in quiescence.) Dividing the bright LMXB number per solar mass by the quiescent NS LMXB per solar mass, we get lower limits on the quiescent NS LMXB duty cycle. Using the Milky Way numbers, we find a duty cycle lower limit of ~ 0.003 , while using the two LMXBs in the LMC we find 0.0005. These limits are consistent with the estimates of NS LMXB duty cycles given in section 3.7, though they are not far

below the lowest estimates, e.g. 0.005-0.01 for GRS 1915+105 [100].

This result can also be interpreted as placing a limit on the size of any quiescent NS LMXB populations that never engage in bright LMXB outbursts, but keep their NSs hot through more frequent lower-level accretion, such as very faint X-ray transients [99]. Using the Milky Way’s bright LMXB frequency, and taking a 10% “canonical” duty cycle for normal LMXBs, we can constrain any such population to be no more than ~ 30 times larger than the normal LMXB population, with appropriate caveats.

Chapter 7

Conclusion:

In this work we have studied the X-ray sources in the Deep Field 1 and Deep Field 2 regions in the Small Magellanic Cloud, a satellite galaxy of the Milky Way, to search for NS LMXBs between outbursts, in the quiescent state. We have investigated the XRSs by reducing the Chandra data and performing source detection using CIAO, and extracting data using ACIS_EXTRACT. We create an X-ray color-magnitude diagram (XCMD) for identifying NS quiescent LMXBs through their luminosity and X-ray color. In plotting our XCMDs for both fields, we found 10 possible candidate quiescent LMXBs which have relatively soft spectra (within the 2σ of the NS atmosphere tracks) and L_x in the range of $6 \times 10^{32} \text{ ergs}^{-1}$ to $10^{34} \text{ ergs s}^{-1}$. These sources are analysed and constrained through our work to determine whether they may be NS qLMXBs.

We start with the spectral fitting of those ten sources. Three XSPEC models: a simple power law, a thermal plasma MEKAL spectrum and a two component model of a hydrogen-atmosphere NS model together with a power law, are fitted on all our nine sources. For the low counts (< 40) of most of our sources we have used C-statistics with Monte Carlo simulation of the best fit spectrum rather than χ^2 -statistics. In the

power law fitting we have seen three sources (005232.28-722607.7, 005339.39-722732.3, and 005010.02-731931.3) are poorly fitted while two sources (005320.49-722349.3 and 005334.39-722236.8) showed a requirement of $\Gamma \gg 2$. These five candidates have relatively soft spectra, and may be chromospherically active stars, or quiescent NS LMXBs. For two component model (power-law+nsatmos) fitting we found that one of these five sources 005010.02-731931.3 has no signature of a NS atmosphere component in its spectrum, indicating that we cannot show that it is a quiescent NS LMXB. From MEKAL fitting two sources (005232.28-722607.7 and 005320.49-722349.3) are not well-fit by single-temperature thermal plasma spectral fits, which suggests they are not chromospherically active stars. The other two remaining candidates (005334.39-722236.8 and 005339.39-722732.3) can be fit by MEKAL models, making chromospherically active stars a possibility for these two sources.

To identify the soft X-ray sources produced by nearby chromospherically active stars which may show relatively bright star signature in existing catalogues, we used the work of Antoniou et al. (2009) for identifying optical counterparts of our nine candidates in the SMC. We found matching optical counterparts for two sources- 005010.02-731931.3 as a Be XRB with relatively soft spectrum to be in quiescence and 005355.38-722645.3 as an AGN in the SIMBAD Astronomical database.

Quiescent NS LMXBs shows higher ratios of the X-ray flux to optical flux than any other known GC source class [90,91]. In chap 5.4 we have found a range of lower limits on $\frac{F_x}{F_{opt}}$ from 0.35 down to 0.035 for the unidentified sources while optically identified sources 005010.02-731931.3 gave 0.4 and 005355.38-722645.7 showed 0.009. We know that qLMXBs with known optical counterparts have typical $(\frac{F_x}{F_{opt}})$ ratios of 10 while $(\frac{F_x}{F_{opt}})_{CV} \sim 1$, and $(\frac{F_x}{F_{opt}})_{activebinaries} < 1$ with the vast majority below 0.01 [90]. As CVs and active binaries with $L_x > 10^{32} \text{ergs}^{-1}$ have very hard spectra, so they are

out from our consideration but polar CVs have soft spectra at these L_X values, and also have high $\frac{F_x}{F_{opt}}$. Moreover, faint M-dwarfs can have $(\frac{F_x}{F_{opt}})_{max}$ up to ~ 1 [85] so we also cannot rule out them completely from our $\frac{F_x}{F_{opt}}$ results.

So far we have five reasonable candidates of quiescent NS LMXBs (CXOU J005232.28-722607.7, CXOU J005320.49-722349.3, CXOU J005339.39-722732.3, CXOU J005401.03-722411.0) and CXOU J005340.68-72300.83 but we cannot rule out other possibilities like polar CVs in the SMC, and M dwarfs in our galaxy. In chapter 6.1 we computed the fraction of quiescent NS LMXBs that could be detectable in our survey. We have estimated $\sim 10\%$ of the quiescent NS LMXBs in the SMC can be detectable. In chapter 6.2 we have calculated the amount of stellar mass that we have surveyed in the SMC using 2MASS and IPAC's Gator service, finding a surveyed stellar mass of $4.4 \times 10^7 M_\odot$ in the two deep fields. As we have detected 4 quiescent NS LMXBs, and were sensitive to 10% of these LMXBs in our surveyed area, then we can make a rough estimate $\frac{50}{4.4 \times 10^7} \sim 10^{-6}$ quiescent NS LMXBs per solar mass in the SMC which could be the upper limit on the number of quiescent NS LMXBs in SMC. As no bright LMXBs are detected in the SMC yet, we consider the LMXB population of the Milky Way and LMC to calculate the duty cycle of quiescent NS LMXBs. In chap 6.3 we have found a duty cycle lower limit of ~ 0.003 using the Milky Way numbers while ~ 0.0005 using LMC LMXBs population. This result can also be interpreted as placing a limit on the size of any quiescent NS LMXB populations that never engage in bright LMXB outbursts, but keep their NSs hot through more frequent lower-level accretion.

Overall, this thesis has shown the upper limit on the number of quiescent NS LMXBs in SMC using our detection of 4 probable candidates of quiescent NS LMXBs.

Bibliography

- [1] F. D. Seward & P. Charles ,Exploring the X-ray Universe (2010).
- [2] M. A. Seeds, Foundation of Astronomy (2010).
- [3] B. A. Carroll & D. A. Ostlie (2007).
- [4] Pallavicini, R., Golub., L., Rosner, R., et al. , ApJ, **248**, 279(1981)
- [5] Schatzman, E., Annales Astrophys., **25**, 18(1962)
- [6] Dan Maoz , Astrophysics in a nutshell(2007)
- [7] N. E. White , F. Nagase & A. N. Parmar (1995) , X-ray binaries, ed. W. H. G. Lewin, J. van Paradijs, & E. P. J. van den Heuvel (Cambridge University Press)
- [8] Smith R. C., 2007, arXiv:astro-ph/0701654v1
- [9] Howell, S. B., Nelson, L. A., & Rappaport, S., ApJ, **550**, 897(2001)
- [10] Patterson, J., ApJS, **54**, 443(1984)
- [11] Gansicke, B. et al., MNRAS, **397**, 2170(2009)

- [12] Kaper, L., van der Meer, A., & Tijani, A. H. 2004, in *Revista Mexicana de Astronomia y Astrofisica Conference Series*, Vol. 21, *Revista Mexicana de Astronomia y Astrofisica Conference Series*, ed. C. Allen & C. Scarfe, 128131
- [13] Liu, Q. Z., van Paradijs, J., & van den Heuvel, E. P. J., *A & AS*, **147**, 23(2000)
- [14] Liu, Q. Z., van Paradijs, J., & van den Heuvel, E. P. J., *A & AS*, **368**, 1021(2001)
- [15] Sparke, L. S. & Gallagher, III, J. S. 2000, *Galaxies in the universe : an introduction* (Cambridge University Press)
- [16] Haberl, F., & Pietsch, W. 2008b, *A&A*, **484**, 451
- [17] Hobbs G., Lorimer D. R., Lyne A. G., Kramer M., *MNRAS*, **360**, 974(2005)
- [18] Cumming, A., Zweibel, E., & Bildsten, L. 2001, *ApJ*, **557**, 958
- [19] S. A. Balbus and J. F. Hawley, "Instability, Turbulence, and Enhanced Transport in Accretion Disks," *Reviews of Modern Physics*, **70**, 1 (1998)
- [20] Frank, J., King, A.R., & Raine, D.J. 1992, *Accretion Power in Astrophysics*, Second edition (Cambridge University Press)
- [21] Campana, S., Colpi, M, Mereghetti, S., Stella, L., & Tavani, M., *A&ARv*, **8**, 279(1998)
- [22] Wijnands R, Craig O. Heinke, D. Pooley, P. D. Edmonds, W. H.G. Lewin, J. E. Grindlay, P. G. Jonker & M. Miller , *ApJ.*, **618**,883 (2005)
- [23] Rutledge, R. E., Bildsten, L., Brown, E. F., Pavlov, G. G., & Zavlin, V. E., *ApJ*, **578**, 405 (2002)

-
- [24] Grindlay, J. E., Heinke, C. O., Edmonds, P. D., & Murray, S. S., *Science*, **292**, 2290 (GHE01)(2001)
- [25] Edmonds, P., Gilliland, R., Heinke, C., & Grindlay, J., *ApJ*, **596**, 1177 & 1197 (2003)
- [26] Brown, E. F., Bildsten, L., & Rutledge, R. E., *ApJ*, **504**, L95(1998)
- [27] Zavlin, V. E., Pavlov, G. G., & Shibano, Yu. A., *A&A*, **315**, 141(1996)
- [28] McClintock, J. E., Narayan, R., & Rybicki, G. B., *ApJ*, **615**, 402(2004)
- [29] Heinke, C. O., Rybicki, G. B., Narayan, R., & Grindlay, J. E., *ApJ*, **644**, 1090(2006)
- [30] Grimm, H.-J., Gilfanov, M., Sunyaev, R., *A&A*, **391**, 923(2002)
- [31] H.-J. Grimm, J. McDowell, A. Zezas, D.-W. Kim & G. Fabbiano, *ApJS*, **173**, 70(2007)
- [32] van Paradijs, J., *ApJ*, **464**, L139(1996)
- [33] King, A. R., Kolb, U., & Burderi, L., *ApJ*, **464**, L127(1996)
- [34] Dubus, G., Lasota, J., Hameury, J., & Charles, P., *MNRAS*, **303**, 139(1999)
- [35] Menou, K., Perna, R., & Hernquist, L., *ApJ*, **564**, L81(2002)
- [36] Q.Z. Liu, J. van Paradijs, E.P.J. van den Heuvel *A&A*, **469**, 807 (2007).
- [37] Wijnands R., Miller J.M., Markwardt C., Lewin W. H. G., van der Klis M., *Ap. J. Lett*, **560**, L159(2001)

- [38] Binney, J., & Merrifield, M., Galactic Astronomy (Princeton: Princeton Univ. Press)(1998)
- [39] Fabian, A.C., Pringle, J.E., & Rees, M.J., MNRAS, **172**, 15(1975)
- [40] Hills, J. G., AJ, **80**, 1075(1975)
- [41] Clark, G. W., ApJ, **199**, L143(1975)
- [42] Katz, J. I., Nature, **253**, 698
- [43] Verbunt, F., Elson, R.,& van Paradijs, J., MNRAS, **210**, 899(1984)
- [44] Pooley, D., et al., ApJ, **569**, 405(2002a)
- [45] Pooley, D., Blackburne, J. A., Rappaport, S., Schechter, P. L., & Fong, W., ApJ, **648**, 67(2006)
- [46] Heinke, C.O., Grindlay, J.E., Lugger, P.M., Cohn, H.N., Edmonds, P.D., Lloyd, D.A., & Cool, A.M., ApJ,**598**, 501(2003)
- [47] in 't Zand, J.J.M., Jonker, P.G., Markwardt, C.B., Astronomy & Astrophysics, **465**, 953(2007)
- [48] Cackett, E. M., Brown, E. F., Miller, J. M., & Wijnands, R., ApJ, **720**, 1325(2010)
- [49] Campana, S. et al., ApJ, 575, L15(2002)
- [50] Heinke, C. O., Jonker, P. G., Wijnands, R., & Taam, R. E., ApJ, 660, 1424(2007)

- [51] Verbunt, F. & Lewin, W. H. G. 2006, Globular cluster X-ray sources (Compact stellar X-ray sources, ed. L. Walter, & M. van der Klis, Cambridge Astrophysics Series, No. 39 (Cambridge, UK: Cambridge University Press), 341
- [52] Lewin, W. H. G., van Paradijs, J., & Taam, R. E., X-ray Binaries, ed. W. H. G. Lewin, J. van Paradijs, & E. P. J. van den Heuvel (Cambridge Univ. Press), 175(1995)
- [53] in 't Zand, J., Hulleman, F., Markwardt, C., & et al., A&A, **406**, 233(2003)
- [54] C. O. Heinke , J. E. Grindlay , & P. D. Edmonds, ApJ, 622:556-564, (2005)
- [55] Voss, R., & Gilfanov, M., A&A, **468**, 49(2007)
- [56] Heinke, C. O., Altamirano, D., Cohn, H. N., Lugger, P. M., Budac, S. A., Servillat, M., Linares, M., Strohmayer, T. E., Markwardt, C. B., Wijnands, R., Swank, J. H., Knigge, C., Bailyn, C., & Grindlay, J. E., ApJ, **714**, 894(2010)
- [57] Jonker, P. G., & Nelemans, G., MNRAS, **354**, 355(2004)
- [58] Pooley, D., Homan, J., Heinke, C., et al., ATel, **2974**, 1(2010)
- [59] Pooley, D., Lewin, W., Anderson, S., & et al., ApJ, **591**, L131(2003)
- [60] Maccarone, T. J., Gallo, E., & Fender, R., MNRAS, **345**, L19(2003)
- [61] Maccarone, T., Fender, R., & Tzioumis, A., Ap&SS, **300**, 247(2005)
- [62] Sarazin, C., Kundu, A., Irwin, J., & et al., ApJ, **595**, 743(2003)
- [63] Deutsch, E. W., Margon, B., and Anderson, S. F., Astrophys. J. Lett., **530**, L21L24,(2000).

-
- [64] D. R. Zurek, C. Knigge, T. J. Maccarone, A. Dieball & K. S. Long., *ApJ*, **699**, 1113(2009)
- [65] Altamirano, D., Cavecchi, Y., et al., arXiv:1005.3527 (2010)
- [66] N. Ivanova , K. Belczynski, J.M. Fregeau, & F.A. Rasio , *ApJ*, **621**, L105 (2005)
- [67] Hertz, P., & Grindlay, J., *ApJ*, **275**, 105(1983)
- [68] Cool, A., Grindlay, J., Cohn, H., Lugger, P., & Slavin, S., *ApJ*, **439**, 695(1995)
- [69] Saito, Y., Kawai, N., Kamae, T., & et al., *ApJ*, **477**, L37(1997)
- [70] C. O. Heinke et al. ,2011, in preparation.
- [71] Harris, J. & Zaritsky, D.AJ, **127**, 1531(2004)
- [72] Dan Coe, Narciso Benitez, Tom Broadhurst, and Leonidas A. Moustakas, *ApJ*, **722**, 125, (2010)
- [73] V. Antoniou, A. Zezas, D. Hatzidimitriou & J. C. McDowell, *ApJ*, **697**, 1695(2009)
- [74] McSwain, M. V. & Gies, D. R., *ApJS*, **161**, 118(2005)
- [75] Laycock, S., Tang, S., Grindlay, J., Los, E., Simcoe, R., & Mink, D., *AJ*, 140 (2010)
- [76] Laycock, S., Corbet, R. H. D., Coe, M. J., et al., *ApJS*, **161**, 96(2005)
- [77] Mukherjee, U., & Paul, B., *A&A*, **431**, 667 (2005)
- [78] Broos, P. S., et al., *Ap J.*, **714** 1582-1605 (2010)

- [79] Taylor, A. R., et al., *AJ*, **125**, 3145(2003)
- [80] Laycock S., Zezas G., & Hong J., *astro-ph/0809.1738*(2008)
- [81] Cash, W., *ApJ*, **228**, 939 (1979)
- [82] C. O. Heinke, R. Wijnands, H. N. Cohn, P. M. Lugger, J. E. Grindlay, D. Pooley, & W. H. G. Lewin, *ApJ*, **651**, 1098-1111(2006)
- [83] Heinke, C. O., Grindlay, J. E., Edmonds, P. D., Cohn, H. N., Lugger, P. M., Camilo, F., Bogdanov, S., & Freire, P. C., *ApJ*, **625**, 796(2005b)
- [84] Liedahl, D. A., Osterheld, A. L., & Goldstein, W. H., *ApJ*, **438**, L115(1995)
- [85] J.H.M.M. Schmitt & C. Liefke, *A&A*, **417**, 651-665 (2004)
- [86] Schmitt, J.H.M.M., Fleming, T.A. and Giampapa, M.S., *Ap.J.* **450**, 392.
- [87] Sparke, L. S. & Gallagher, J., *Galaxies in the Universe*, Cambridge University Press(2007)
- [88] Udalski, A., Soszynski, I., Szymanski, M., Kubiak, M., Pietrzynski, G., Wozniak, P., & Zebrun, K., *Acta Astronomica*, 48, 563(1998b)
- [89] Zaritsky, D., Harris, J., Thompson, I. B., Grebel, E. K., & Massey, P., *AJ*, **123**, 855(2002)
- [90] Edmonds, P. D., Gilliland, R. L., Heinke, C. O., & Grindlay, J. E., *ApJ*, **596**, 1197 (2003b)
- [91] Bassa, C., Pooley, D., Homer, L., et al., *ApJ*, **609**, 755(2004)

-
- [92] Heinke, C. O., Grindlay, J. E., Edmonds, P. D., Cohn, H. N., Lugger, P. M., Camilo, F., Bogdanov, S., & Freire, P. C., *ApJ*, **625**, 796(2005b)
- [93] G. Coomber, C. O. Heinke, H. N. Cohn, P. M. Lugger, & J. E. Grindlay, in preparation(2011)
- [94] Skrutskie, M. F., et al., *AJ*, **131**, 1163(2006)
- [95] Wood, P. R. ,*Astrophysics & Space Science* , **217**, 121-130(1994)
- [96] Bekki K., Stanimirovic S., *MNRAS*, **395**, 342(2009)
- [97] Andrew Gould, 1998, *Galactic Structure From Infrared Surveys*, arXiv:astro-ph/9808083v1
- [98] Ramsay, G., & Cropper, M.,, *MNRAS*, **338**, 219(2003)
- [99] Wijnands, R., int Zand, J. J. M., Rupen, M., et al., *A&A*, **449**, 1117(2006a)
- [100] Deegan, P., Combet, C., & Wynn, G. A., *MNRAS*, in press(2009), (arXiv:0908.2566)
- [101] Verbunt, F. & Hut, P. 1987, in *The Origin and Evolution of Neutron Stars*, IAU Symposium No. 125, ed. D. Helfand & J.-H. Huang (Dordrecht: Reidel), 187-197
- [102] T. Fragos et al., *ApJ* **702**, L143(2009)
- [103] Pooley, D., Blackburne, J. A., Rappaport, S., Schechter, P. L., & Fong, W., *ApJ*, **648**, 67(2006)
- [104] Colpi, M., Geppert, U., Page, D., & Possenti, A., *ApJ*, **548**, L175(2001)